Chem Soc Rev

REVIEW ARTICLE

View Article Online
View Journal | View Issue



# Metal–metalloporphyrin frameworks: a resurging class of functional materials

Cite this: *Chem. Soc. Rev.*, 2014, **43**, 5841

Wen-Yang Gao, Matthew Chrzanowski and Shengqian Ma*

Received 1st January 2014

DOI: 10.1039/c4cs00001c

www.rsc.org/csr

This review presents comprehensively recent progress in metal–metalloporphyrin frameworks (MMPFs) with an emphasis on versatile functionalities. Following a brief introduction of basic concepts and the potential virtues of MMPFs, we give a snapshot of the historical perspective of MMPFs since 1991. We then summarize four effective strategies implemented frequently to construct prototypal MMPFs. MMPFs represent a resurging class of promising functional materials, highlighted with diverse applications including guest-molecule adsorption and separation, catalysis, nano-thin films and light-harvesting.

## 1. Introduction

As this part of a themed issue involving metal–organic frameworks (MOFs), also known as coordination polymers, general backgrounds on MOFs and their applications will not be provided,[1–3] other than where closely relevant to metal–metalloporphyrin frameworks (MMPFs). In the wide horizons of MOFs studies, metal–metalloporphyrin frameworks (MMPFs) arouse intensive research interest, although MMPFs still remain in their premature stage.

The driving force behind the rapid growth of MMPFs is twofold. On one hand, an important motivation lies in such remarkable features of porphyrin and metalloporphyrin molecules as their highly thermal and chemical stabilities, robust nature, and facile synthesis.[4–7] Porphyrins and metalloporphyrins thus afford great potential as building blocks in the construction of coordination polymers in analogy to robust inorganic zeolites for versatile applications. On the other hand, metalloporphyrins are one of the cornerstones on which the existence of life is based, and essential biochemical, enzymatic, and photochemical functions depend on the special properties of the tetrapyrrolic macrocycle.[5] Given the ubiquitous biological functions of metalloporphyrins in nature (for example light-harvesting, oxygen transportation and catalysis), building coordination architectures using custom-designed porphyrin ligands becomes exceedingly desirable in pursuance of mimicking their diverse biological functionalities.

MMPFs compose a class of coordination networks self-assembled *via* judicious selection of metal-containing secondary building units (SBUs) and custom-designed metalloporphyrin ligands.

*Department of Chemistry, University of South Florida, 4202 East Flower Avenues, Tampa, Florida, USA. E-mail: sqma@usf.edu; Fax: +1-813-974-3203; Tel: +1-813-974-52217*

**Wen-Yang Gao**

*Wen-Yang Gao was born in Shandong, China in 1989. He received his BS degree with honors from Sun Yat-sen University, China in 2011. During his undergraduate years, he carried out MOFs research under the supervision of Dr Long Jiang and Dr Tong-Bu Lu. In the fall of 2011, he joined the research group of Professor Shengqian Ma to pursue his PhD degree at the University of South Florida. His research focuses on the development of functional porous MOFs including porous metalloporphyrin-based materials for catalysis application.*

**Matthew Chrzanowski**

*Matthew Chrzanowski obtained his BS in Chemistry from the University of South Florida (USF) in 2012 and began his PhD studies at USF that same year. Since 2010, he has been performing research under the supervision of Professor Shengqian Ma. His research focuses on the development of novel functional porous porphyrin based frameworks by exploiting the versatility of porphyrin complexes for biomimetic, heterogeneous catalysis, and gas storage and separation processes.*

The porphyrin core allows pre-metalation, metalation *in situ* or postmetalation by numerous metal ions generating metalloporphyrin-based networks. However, in order to facilitate the discussion below, we extend MMPFs to the MOFs integrating either porphyrin or metalloporphyrin struts as their linkers. Meanwhile, MOFs that encapsulate porphyrin or metalloporphyrin molecules within frameworks as guest molecules have been excluded from the following content.

This review focuses on recent progress on metal–metalloporphyrin frameworks with an emphasis on the versatile functionalities investigated by our group and others. MMPFs have demonstrated great potential for diverse applications, such as guest molecule adsorption and separation, catalysis, nanothin films and light-harvesting. The purpose of our review is to provide a concise survey of a plethora of reported investigations in this area. Our target is to not detail all the work to date but rather to systematize the major and seminal achievements and reflect on current research.

The review is divided into four main sections. First of all, the historical perspective of MMPFs briefly introduces porphyrin-based coordination polymers developed since 1991. Then, four effective strategies frequently implemented to build up functional MMPFs are summarized. Thirdly, the review gives a comprehensive study of the versatile functionalities of porphyrin based MOFs and relates those functionalities to different applications. Finally, concluding remarks and future prospects are carefully examined through reflection on current research progress.

## 2. Historical perspective

The first porphyrin-based coordination polymer was reported by Robson and co-workers in 1991,[8] far earlier than the benchmarks of MOFs, HKUST-1[9] and MOF-5.[10] In this report, palladium-based tetrapyridyl porphyrin ligands were interconnected into an infinite 3-dimensional framework through coordination to cadmium ion nodes, shown in Fig. 1. This structure also represents the first heterometallic MOF considering that the metal coordinated in the porphyrin cores differs from the metal composing the structural nodes. Furthermore, it was predicted in the report that utilizing metalloporphyrins as slab-like components would be especially attractive to construct new infinite structures due to the stability, rigidity, and potential for 4-connecting symmetry of metalloporphyrins. Shortly thereafter in the same year, Fleischer and co-workers documented a zigzag chain (1D) coordination polymer synthesized *via* self-assembly of a zinc-based 5-pyridyl-10,15,20-triphenyl porphyrin.[11]

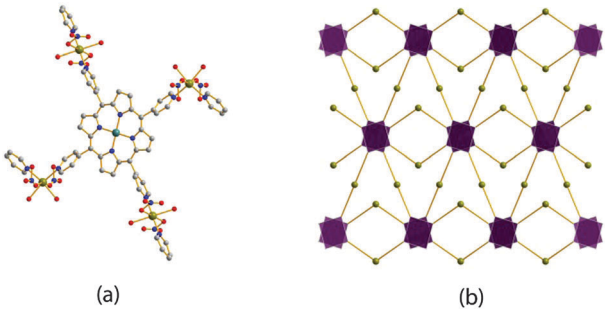


Fig. 1 (a) A view of the Pd-based porphyrin ligand and the attached cadmium center; (b) a representation of the extended 3D framework.

The initial studies about porphyrin-based coordination polymers triggered a plethora of 1D, 2D and 3D MMPFs according to the literature survey. The synthesis of porphyrinic framework solids has seen major contributions from Goldberg,[12–40] Suslick,[41–45] Choe,[46–59] Hupp,[60–66] Zhou,[67–70] Wu,[71–77] Ma[78–85] and others.[8,86–91] The brief history of the early stages cannot individualize all the MMPFs work; hence the well-recognized and seminal work is discussed as follows from our perspective.

Although many single crystal structures of MMPFs exhibit pores fraught with disordered solvent molecules, very few of them can maintain their structural integrity upon removal of solvates. Lin, in 1999, presented the first metalloporphyrin-based MOF stable after the removal of solvent molecules, built by tetra(4-pyridyl)porphyrin and Co(II) or Mn(II) metal ions that generated a 3D framework possessing large cavities.[92] The frameworks, illustrated in Fig. 2, retained their structures, confirmed by powder X-ray diffraction after removal of solvent molecules and after immersion in boiling crude oil for several hours. The structure's high stability results from the axial coordination of two adjoining porphyrin pyridyl groups on the porphyrin metal centers, creating a complex network highly supportive structure. However, since both axial coordination sites on the porphyrin ring were occupied, no accessible open metal centers allowed for further functionality studies.

Suslick and co-workers published the first functionality study of a porphyrin-based coordination polymer in 2002, when selective sorption of guest solvent molecules was examined.[43] The metalloporphyrin network [CoT($p$-$CO_2$)PP$Co_{1.5}$], denoted PIZA-1, was fabricated *via* self-assembly of cobalt chloride and free-base *meso*-tetra(4-carboxyphenyl)porphine under solvothermal conditions. During the self-assembly reaction, the porphyrins were metallated *in situ* by Co(III) ions. PIZA-1, a

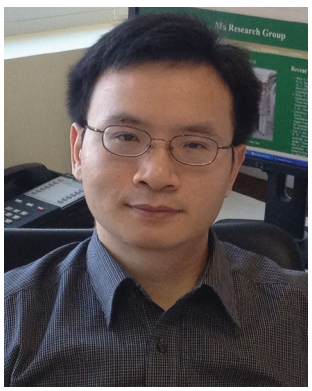

**Shengqian Ma**

*Dr Shengqian Ma received his BS degree from Jilin University, China in 2003, and graduated from Miami University (Ohio) with a PhD degree under the supervision of Hong-Cai Joe Zhou (currently at Texas A&M University) in 2008. After finishing two-year Director's Postdoctoral Fellowship at Argonne National Laboratory, he joined the Department of Chemistry at University of South Florida as an Assistant Professor in August 2010. His current research interests focus on the development of functional porous materials for energy, biological, environmental-related applications.*

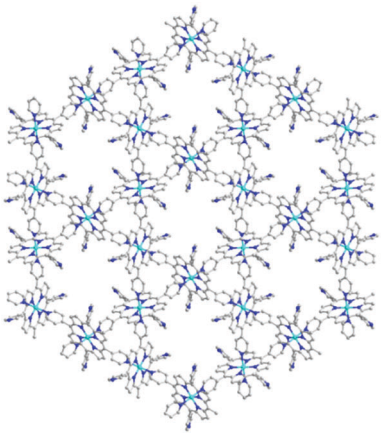

Fig. 2 Perspective view of the first stable metalloporphyrinic framework upon solvent removal.

stable and robust framework, demonstrates a large void volume composed of hydrophilic channels accessible to guest molecules (Fig. 3). The porphyrin metal centers lined and functionalized the walls of the channels. Hence PIZA-1 displayed repeatable size-, shape- and functional group-selective sorption towards a series of solvent guest molecules. The results from this work indicate the feasibility using porphyrin molecules as building blocks for the rational construction of functional

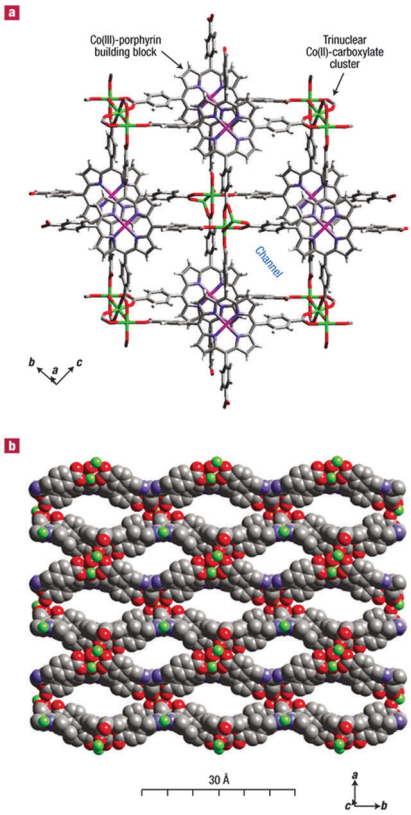


Fig. 3 Molecular diagrams of the PIZA-1 network. Reprinted (adapted) with permission from ref. 43. Copyright © 2002, rights managed by Nature Publishing Group.

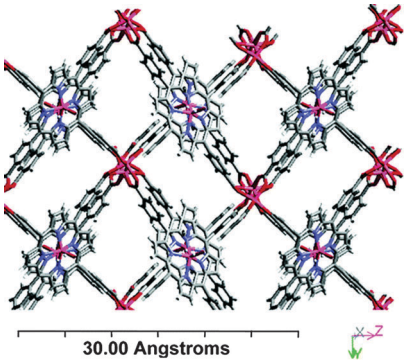


Fig. 4 The PIZA-3 network viewed along the *a*-axis. Reprinted (adapted) with permission from ref. 45. Copyright © 2005, American Chemical Society.

porous solids, while inspiring the exploration of these functional materials as size- and shape-selective heterogeneous catalysts.

Metalloporphyrins have been well established as excellent homogeneous catalysts for hydroxylation of alkanes and epoxidation of alkenes.[5] With respect to the above-mentioned selective sorption studies, porous metalloporphyrin networks have the appealing potential to act as size- and shape-selective heterogeneous catalysts. Despite the great potential for heterogeneous catalysts, the first catalytic study performed on metalloporphyrin-based MOFs occurred in 2005 when Suslick and co-workers demonstrated that PIZA-3 (shown in Fig. 4) acted as a heterogeneous catalyst.[45] PIZA-3 contains manganese(III) tetra-(*p*-carboxyphenyl)porphyrins that coordinate to a bent trinuclear manganese cluster. PIZA-3 proved a capable and robust oxidation catalyst for the hydroxylation of a variety of linear and cyclic alkanes and the epoxidation of cyclic alkenes. However, the microporous channels constrain substrate molecules' diffusion throughout the channels, thus catalysis occurred only on the exterior of the framework, leading to a lack of shape selectivity for the substrate molecules.

Since then, a rapid resurgence in the numbers of porphyrin-based MOF structures reported in the literature has occurred. Particularly, in recent years the number of publications focusing on porphyrin-based MOFs has been exponentially increasing, as shown in Fig. 5. In fact, more research interests emphasize the

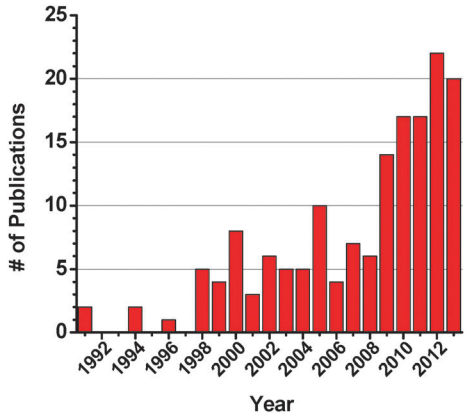


Fig. 5 Number of porphyrinic MOFs publications plotted a function of year.

functionality studies, rather than serendipitous discoveries of porphyrinic networks. In Scheme 1, we summarize all the porphyrin-derived organic ligands used to construct frameworks.[11,17,31,35,44,46,52,60,78,80,81,83,85,86,93–102] The recent advancement of organic synthesis endows the construction of porphyrinic frameworks with custom-designed ligands, which further allows optimization of the pore structure, surface functions, and other properties for specific applications as porous materials.

# 3. Synthetic strategies

A plethora of porphyrin- or metalloporphyrin-based coordination polymers have been widely established and, like all other coordination polymers, can be categorized as 1D chains, 2D grids and 3D nets. Choe and co-workers published one review article examining systematically the classification of structural motifs in porphyrinic networks assembled from 5,10,15,20-tetrapyridylporphyrin and its derivatives.[51] Despite the fact that prior predication of the assembled coordination networks remains a colossal challenge, it is still feasible to formulate rationally plenty of MOFs by virtue of the custom-design of organic ligands and judicious selection of metal-containing SBUs. In the following section, we discuss intensively four effective synthetic strategies frequently implemented to construct metalloporphyrinic frameworks.

## 3.1 Crystal engineering

Crystal engineering[103,104] provides an effective means for the targeted formulation of a wide range of extended metalloporphyrin-based architectures with preconceived structures and desirable properties, on the basis of intermolecular interactions, especially coordination bonds. The significance of crystal engineering lies in achieving ordered materials with predefined dimensionality and connectivity *via* the deliberate synthesis strategies.

The first successful example of applying a crystal engineering approach to devising targeted porphyrin/metalloporphyrin-based frameworks appeared in 1994 from Robson and co-workers.[86] The work demonstrated that porphyrin building blocks can be engineered to construct three-dimensional networks with a predicted topology of the **pts** structure, containing large channels. The **pts** prototype net consists in essence of equal numbers of tetrahedral and square-planar centers, each one being connected to four of the other type. Cu(I) provides the tetrahedral center and the square-planar building block is provided by metalloporphyrin units (hereafter 5,10,15,20-tetra(4-pyridyl)-21*H*,23*H*-porphine copper(II) will be referred to as Cu(II)(tpp) and 5,10,15,20-tetra(4-cyanophenyl)-21*H*,23*H*-porphine copper(II) will be referred to as Cu(II)(tcp)). The Cu(tpp)$CuBF_4$ model proved the intended **pts**-related network assembly (Fig. 6). The framework comprised less than half the volume of the crystal, with the remaining space occupied by highly disordered solvent molecules and anions whose positions could not be defined. In the Cu(tcp)$CuBF_4$ case, a similar packing **pts**-related net formed, however, the network is two-fold interpenetrating. The non-interpenetration of Cu(tpp)$CuBF_4$ was tentatively illustrated by that the required close approach of the Cu(I) centers from separate frameworks is precluded by the four bulky pyridyl units around each metal. Both of these two frameworks failed to survive removal of solvent molecules. Collectively, the results demonstrate that crystal engineering offers great potential to assemble pre-determined networks on the basis of selective molecular building blocks.

Encouraged by early successful examples, the crystal engineering strategy, particularly alluring on a practical level, has been employed to target specific networks. The modularity and amenability of MOFs endowed by crystal engineering have become one of the driving forces behind their rapid development. Moreover, their modular nature implies that the prototypal MOFs can serve as blueprints or platforms for a large variety of derivatives offering controllable pore sizes and tunable pore surfaces.

The work with MMPF-3 by Ma and co-workers exemplifies the use of the crystal engineering approach to building a microporous, catalytically active MMPF with **fcu** topology.[80] This is a topology of particular interest because it forms three types of unique polyhedral cages in Fig. 7, using a custom-designed metalloporphyrin linker. We focus on the role crystal engineering plays in constructing a desirable metalloporphyrin-based network mimicking the prototypal MOF, **fcu**-MOF-1, rather than focusing on the catalytic behavior of MMPF-3. Based upon the previous report, **fcu**-MOF-1 was built from 12-connected cubohemioctahedral supermolecular building blocks (SBBs) of formula $[Co_2(\mu_2\text{-}H_2O)(H_2O)_4]_6(bdc)_{12}$ and benzoimidephenanthroline tetracarboxylate (bipa-tc) linkers. MMPF-3 targets the **fcu** topology using **fcu**-MOF-1 as a blueprint. MMPF-3 with **fcu** topology was successfully engineered *via* incorporation of a custom-designed porphyrin ligand. The featuring active metalloporphyrin units in the framework present the opportunity for catalytic studies, which will be discussed later.

Scheme 1 Porphyrin ligands used in the construction of porphyrinic frameworks (tpyp = 5,10,15,20-tetrakis(4-pyridyl)porphine;[86] mpyp = 5-monopyridyl-10,15,20-triphenylphorphine;[11] *trans*-dpyp = 5,15-dipyridyl-10,20-diphenylporphine;[11] tcp = 5,10,15,20-tetrakis(4-cyanophenyl)porphine;[86] t(3-py)p = 5,10,15,20-tetrakis(3-pyridyl)porphine;[95] tdpap = 5,10,15,20-tetrakis(4,4′-dipyridylaminophenylene)porphine;[102] tmpp = 5,10,15,20-tetrakis(3,4,5-trimethoxyphenyl)porphine;[96] tpps = tetrakis(4-sulfonatophenyl)porphine;[97] *trans*-dcpp = 5,15-di(4-carboxyphenyl)-10,20-diphenylporphine;[52] *cis*-dcpp = 5,10-di(4-carboxyphenyl)-15,20-diphenylporphine;[46] bdcpp = 5,15-bis(3,5-dicarboxyphenyl)porphine;[78] dcdbp = 5,15-bis(3,5-dicarboxyphenyl)-10,20-bis(2,6-dibromophenyl)porphine;[80] bdcbpp = 5,15-bis(3,5-dicarboxybiphenyl)porphine;[101] tcpp = 5,10,15,20-tetrakis(4-carboxyphenyl)porphine;[17] tmcpp = 5,10,15,20-tetrakis(*m*-carboxyphenyl)porphine;[31] tcmopp = 5,10,15,20-tetrakis[4-(carboxymethyleneoxy)phenyl]porphine;[35] tcpep = 5,10,15,20-tetrakis(4-carboxyphenyl)ethynylporphine;[98] tcbpp = 5,10,15,20-tetrakis(4-carboxybiphenyl)porphine;[83] tdcpp = 5,10,15,20-tetrakis(3,5-dicarboxyphenyl)porphine;[81] tbcppp = 5,10,15,20-tetrakis[3,5-bis(4-carboxyphenyl)phenyl]porphine;[100] tdcbpp = 5,10,15,20-tetrakis(3,5-dicarboxybiphenyl)porphine[85]).

 

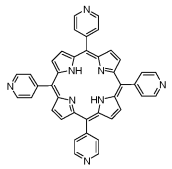
tpyp

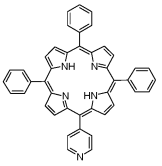
mpyp

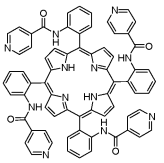

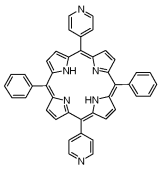
*trans*-dpyp

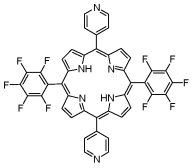

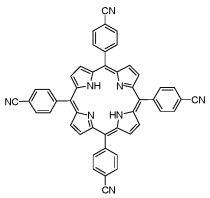
tcp

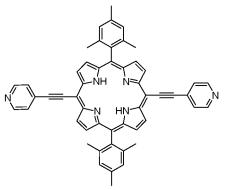

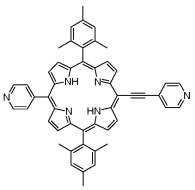

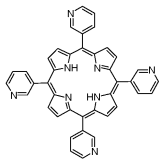
t(3-py)p

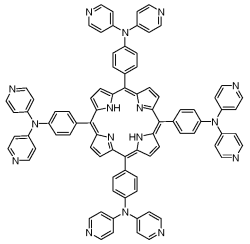
tdpap

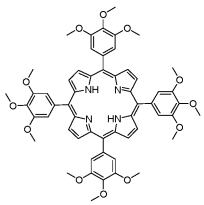
tmpp

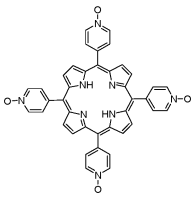

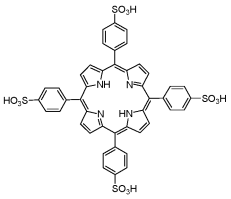
tpps

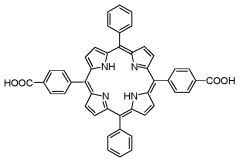
*trans*-dcpp

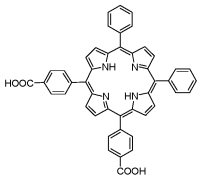
*cis*-dcpp

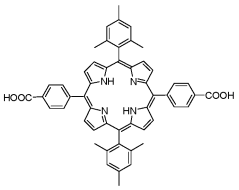

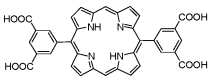
bdcpp

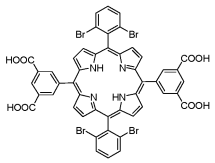
dcdbp

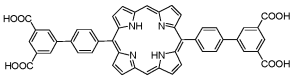
bdcbpp

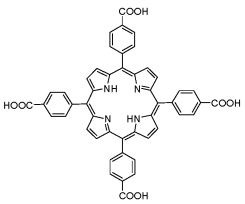
tcpp

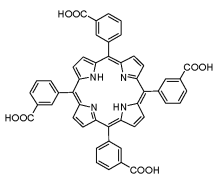
*tm*cpp

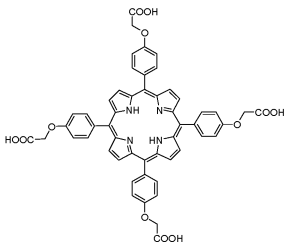
tcmopp

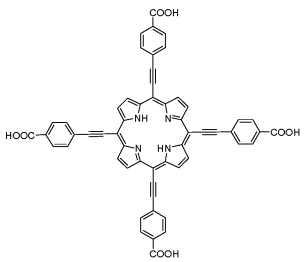
tcpep

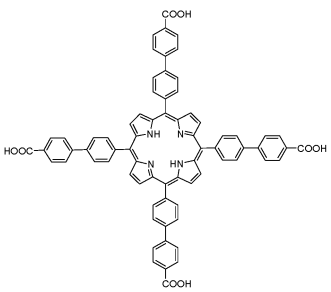
tcbpp

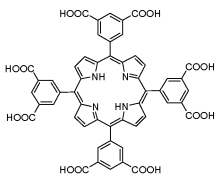
tdcpp

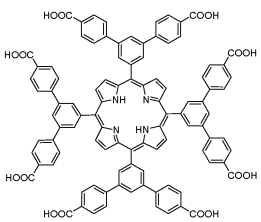
tbcppp

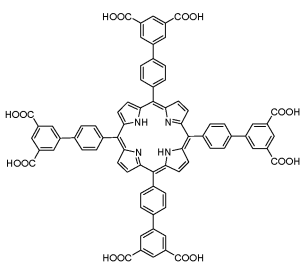
tdcbpp

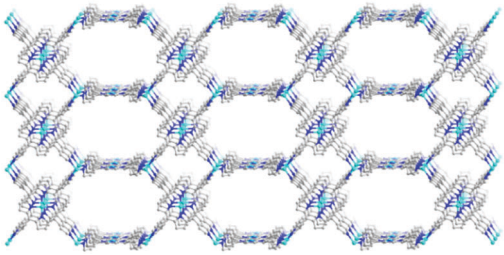

Fig. 6 The extended **pts**-topology structure of $Cu(tpp)CuBF_4$.

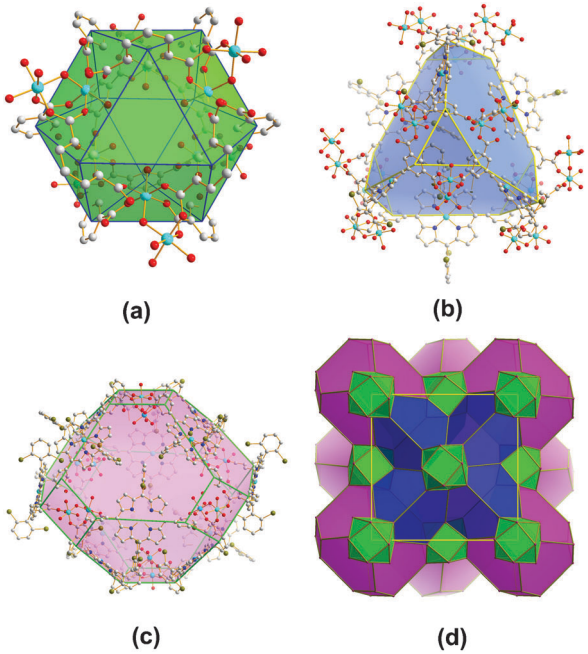


Fig. 7 The three types of polyhedral cages present in MMPF-3: (a) cubohemioctahedron, (b) truncated tetrahedron, and (c) truncated octahedron. (d) 3D structure of MMPF-3 illustrating how its polyhedral cages are connected. Reprinted (adapted) with permission from ref. 80. Copyright © 2012 WILEY-VCH Verlag GmbH & Co. KGaA, Weinheim.

Overall, crystal engineering promises to shift our understanding of the formation of porphyrin-based networks from a process of empirical self-assembly to a rational consideration of custom-designed ligands, SBBs, employing intermolecular forces and other factors. Thus the crystal engineering strategy for the generation of pre-defined networks or the modularity of prototypal blueprints is expected to be a broadly applicable strategy for the development of ordered functional materials.

### 3.2 Pillared-layer strategy

Pillared MOFs, a widely explored platform with numerous applications, consist of two-dimensional layers that have ligating sites for linkage with ditopic pillars, usually dipyridine derivatives, resulting in three dimensional architectures. Functionalizing either the linkers within 2D layers or the ditopic pillared ligands readily tunes the structures and properties of pillared MOFs.

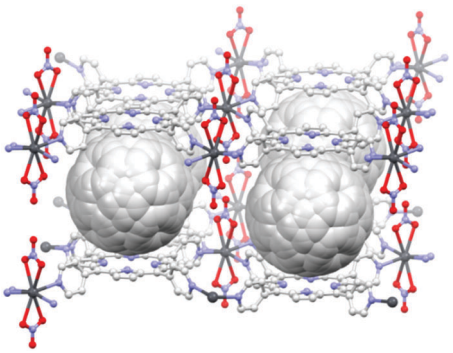

Fig. 8 Crystal packing in pillared-layer structure of fullerene–porphyrin.

The rigidity of metalloporphyrins, together with the square-planar shape of the conjugated tetrapyrrolic macrocycles makes them especially attractive as slab-like components for the construction of two dimensional layers. In 2002, Sun and co-workers reported manipulation of the structures of extended porphyrin systems using fullerene–porphyrin attraction.[105] The $Pb^{2+}$ ions connect the tetra-4-pyridylporphyrins in infinite sheets with an interlayer spacing of 12.1 Å. The fullerenes intercalate between these sheets, acting as pillars, shown in Fig. 8. The fullerenes are precisely centered over the porphyrin cores. Compared to the offset layers in the non-fullerene-containing species, the porphyrins exhibit a strict tetragonal register. This thus indicates that the porphyrin–fullerene supramolecular interaction, a hierarchy of structure-defining elements, ultimately contributes a useful degree of design predictability to fullerene–porphyrin structure assembly. The presented molecular design principles are anticipated to be widely useful in the manipulation of photophysical properties, such as adjusting the charge transfer of molecular conductors.

Combined with specific metal-containing SBUs such as planar paddlewheel units, carboxyphenyl porphyrin ligands tend to form two dimensional layers. These layers form three dimensional pillared-layer networks when interlinked by ditopic pillars of usually dipyridine derivatives. Choe and co-workers conducted a systematic study building a series of porphyrin paddlewheel frameworks (denoted PPFs). The well-established $M_2(COO)_4$ (M = Co, Zn) metal paddlewheel clusters are selected as nodes to bind the porphyrin linkers in the 2D layers. The third components of dipyridyl pillar molecules are incorporated between these layers. The two different metal sites (porphyrin metal site and paddlewheel metal site) available for axial binding induce three possible pillar connection schemes (paddlewheel–porphyrin center; paddlewheel–paddlewheel; porphyrin center–porphyrin center). Meanwhile, different metal ions coordinated in the porphyrin cores can result in different stacking sequences of 2D metalloporphyrinic layers as shown in Fig. 9, due to coordination geometry of incorporated metal ions.[48] For example, the octahedral geometry of cobalt leads to the 6-coordinate node. The tetrahedral geometry of zinc produces a 5-coordinate node, and the square planar geometry of palladium forms a 4-coordinate node. The resulted stacking patterns vary from AB (PPF-3) to ABBA (PPF-4) and

 

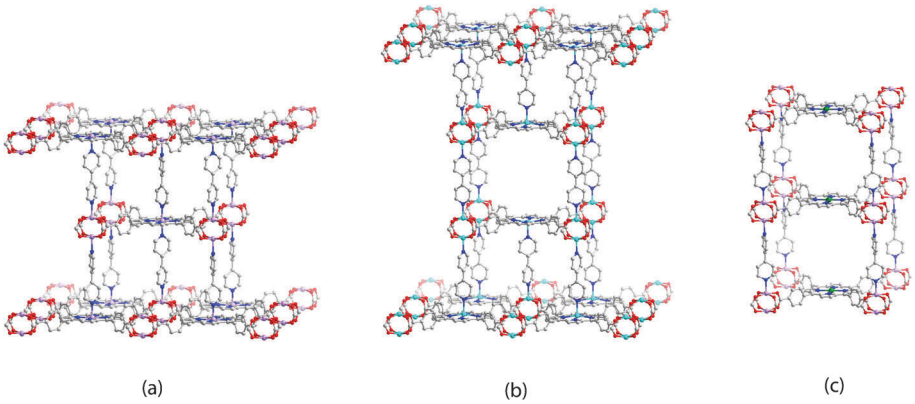


Fig. 9 The 2D sheets are pillared with bipyridine to give (a) PPF-3 (Co, purple), (b) PPF-4 (Zn, turquoise), and (c) PPF-5 (Pd, green).

further to AA (PPF-5). To reserve unsaturated metal sites within the porphyrin cores, a sterically hindered pillar (2,2′-dimethylbipyridine) was selected to coordinate preferentially to paddlewheel metal sites, generating paddlewheel-to-paddlewheel stacking patterns solely.[53]

Instead of using common dipyridyl pillars, dipyridyl porphyrin molecules present an alternative type of pillar to construct functional pillared-layer porphyrinic frameworks. Hupp and co-workers built a series of porphyrinic frameworks with a pillared-layer strategy on basis of dipyridyl porphyrin pillars.[60–66]

### 3.3 Nanoscopic metal–organic polyhedron (MOP)

The construction of metalloporphyrin-based nanoscopic polyhedral cages affords cage walls rich in π-electron density that provide favorable interactions with targeted guests. Such cages also contain multiple active metal centers that could facilitate synergistic interactions with substrates, as exemplified by metalloporphyrin supramolecular materials.[6,7] Considering the escalating interest in constructing metalloporphyrin-based MOFs, metalloporphyrin nanoscopic polyhedral cages built into MOFs allow π-electron-rich cage walls together with a high density of open metal sites confined in the nanospace. This is envisioned to benefit greatly their behavior in versatile applications.

Driven by the above mentioned advantages, in 2011 Ma and co-workers reported the first example of a MOP-based metal–metalloporphyrin framework, MMPF-1, constructed from a custom-designed porphyrin ligand, 5,15-bis(3,5-dicarboxyphenyl)-porphine (bdcpp) and a judiciously selected dicopper paddlewheel SBU, as illustrated in Fig. 10(a).[78] The custom-designed bdcpp ligand features a pair of isophthalates bridged by a porphine macrocycle. Generally the vertex-linking of isophthalate ligands with the square paddlewheel moieties allows the generation of various types of facets MOPs. In this case, eight paddlewheel SBUs are interconnected by sixteen bdcpp ligands to form a nanoscopic cage. Four dicopper paddlewheel SBUs are bridged by four isophthalate moieties from four different bdcpp ligands to form the top of the cage; they are pillared to four dicopper paddlewheel SBUs at the bottom of the cage through eight

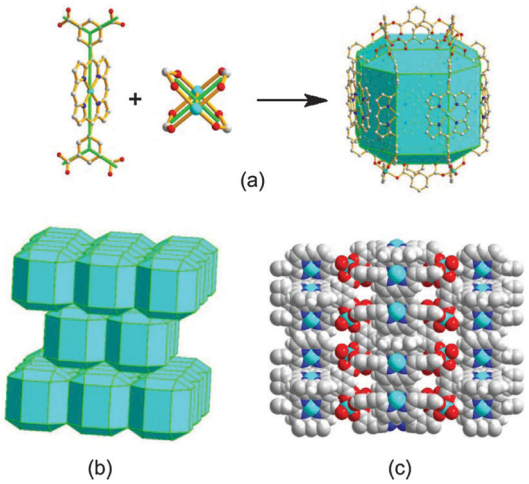


Fig. 10 (a) Illustration of linking the bdcpp ligand and a dicopper paddlewheel to form the irregular rhombicuboctahedral cage; (b) "ABAB" packing of rhombicuboctahedron layers in MMPF-1; (c) space-filling model on the [100] plane indicating the open pore size of ~3.4 Å × 3.5 Å. Reprinted (adapted) with permission from ref. 78. Copyright © 2011, American Chemical Society.

deferent bdcpp ligands. The porphyrin macrocycle of the bdcpp ligand is metalated *in situ* by Cu(II) ion that is free of coordinated solvent molecules, thus leaving both the distal and proximal positions open. In each cage, there are eight open copper sites associated with the porphyrin rings of the bdcpp ligands and eight open copper sites from dicopper paddlewheel SBUs that are activated by thermal liberation of aqua ligands. All 16 open copper sites point toward the center of the cage, creating an unprecedentedly high density of open metal sites in the nanoscopic cage (~7 open metal sites per $nm^3$). By connecting the centers of all isophthalate phenyl rings and the centers of the eight paddlewheels, the polyhedral cage can be depicted as a polyhedron that has 24 vertices, 26 faces, and 48 edges. The MOP serves as an SBB that sustains a 3D porous metalloporphyrin framework structure demonstrating a very high density of open metal sites in the confined nanoscopic polyhedral cage, shown in Fig. 10(b and c).

Soon after the first example of nanoscopic MOP-based porphyrin networks, Ma and co-workers presented a designed

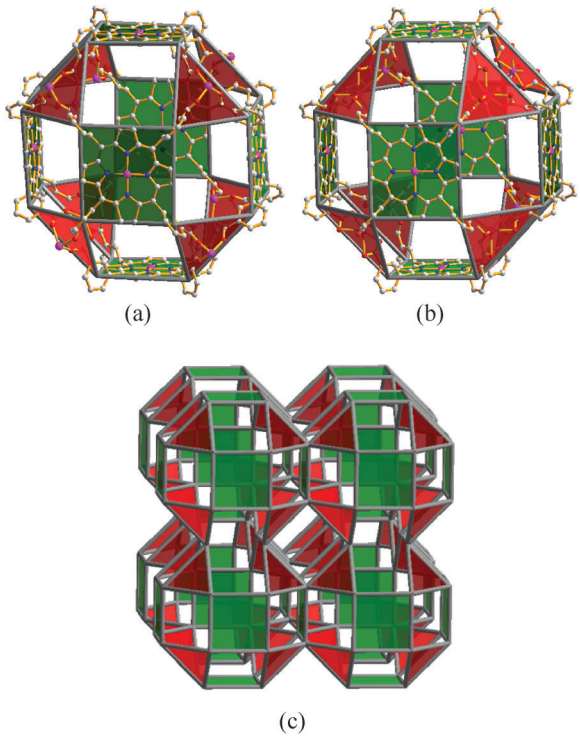


Fig. 11 (a) The small cubicuboctahedron in MMPF-4 is formed by 6-square Zn-tdcpp MBBs and 8-triangular $Zn_2(CO_2)_3$ MBBs; (b) the small cubicuboctahedron in MMPF-5 formed by 6-square Cd-tdcpp MBBs and 8-triangular $Cd(CO_2)_3$ MBBs; (c) the extended 3D framework presented by packing cubicuboctahedral cages. Reprinted (adapted) from ref. 81.

approach to building MMPFs from high connectivity, high symmetry SBBs, that are based upon uniform polyhedra. A custom-designed porphyrin, tetrakis(3,5-dicarboxyphenyl)-porphine (tdcpp) serves as a square molecular building block (MBB) that connect triangular $Zn_2(CO_2)_3$ or $Cd(CO_2)_3$ moieties to form three dimensional frameworks, termed MMPF-4 (Zn) and MMPF-5 (Cd).[81] The small cubicuboctahedron SBBs that are thereby generated *via* vertex-directed self-assembly are the first SBBs that are uniform polyhedra based on porphyrin MMBs. The resulting SBB is a small cubicuboctahedron composed of the faces of six Zn-tdcpp moieties that are linked by eight $Zn_2(CO_2)_3$ moieties, shown in Fig. 11(a). The opposite face of each Zn-tdcpp moiety in MMPF-4 serves as the face of an adjacent SBB, thereby making it 6-connected of a **pcu** net. The cage formed between the SBBs can be described as an octahemioctahedron, and it is enclosed by eight triangular $Zn_2(CO_2)_3$ paddlewheel MBBs from eight different SBBs. The eight triangular $Zn_2(CO_2)_3$ paddlewheel MBBs are bridged through 12 isophthalate moieties from 12 tdcpp ligands nodes. Similarly MMPF-5 is also based upon a small cubicuboctahedron SBB composed of six Cd-tdcpp moieties that are linked by eight $Cd(CO_2)_3$ moieties, shown in Fig. 11(b). SBBs are fused with six adjacent SBBs through six Cd-tdcpp moieties to support an augmented **pcu** network in Fig. 11(c). The high symmetry of the small cubicuboctahedron SBBs distinguishes MMPF-4 and MMPF-5 from MMPF-1, in which cages are formed by pillaring two sets of four copper paddlewheel moieties through eight closely contacted porphyrin ligands. The cages in MMPF-1 therefore possess much lower symmetry compared to those in MMPF-4 and MMPF-5. These high-symmetry porphyrin-based cubicuboctahedral cages were very rare in metalloporphyrin containing frameworks.

In the foregoing discussions, the custom design of porphyrin ligands paves an avenue to build MOP-based frameworks. Meanwhile, the utilization of high symmetry, highly connected metal clusters such as SBUs often display a tendency to achieve frameworks incorporating nanoscopic polyhedral cages, which is well exemplified by MOF-525[106] and PCN-221.[69] MOF-525, reported by Morris *et al.*, is assembled by the 12-connected zirconium cuboctahedral SBU, $Zr_6O_4(OH)_4(CO_2)_{12}$ (Fig. 12(a)), and the commercially available porphyrin ligand, 5,10,15,20-tetrakis(4-carboxyphenyl)porphyrin (tcpp). Two types of polyhedral cages are observed in this structure. The small cage, a slightly distorted octahedron with a cavity diameter of $\sim$1.1 nm, comprises two Zr SBUs in the horizontal direction and four tcpp ligands linked to the two SBUs, illustrated in Fig. 12(b). The other cage, a cube with edge length of $\sim$2.0 nm, consists of eight Zr SBUs at the vertices and six tcpp ligands at the faces (Fig. 12(c)). PCN-221 presents the previously unknown $Zr_8$–$Hf_8$ cubic clusters, shown in Fig. 13(a). The $Zr_8O_6$ cluster features an idealized $Zr_8$ cube, in which each Zr atom resides on one vertex and each face of the cube is capped by one $\mu_4$-O atom. On each edge, two Zr ions are interconnected by a carboxylate from a tcpp ligand to afford a 12-connected SBU. The $Zr_8O_6$ cluster can be generated by exchanging Zr and O atoms with each other in a $Zr_6O_4(OH)_4$ cluster of MOF-525. Similarly, PCN-221 also features two types of polyhedral cages. One of them is composed of two Zr SBUs in the axial direction

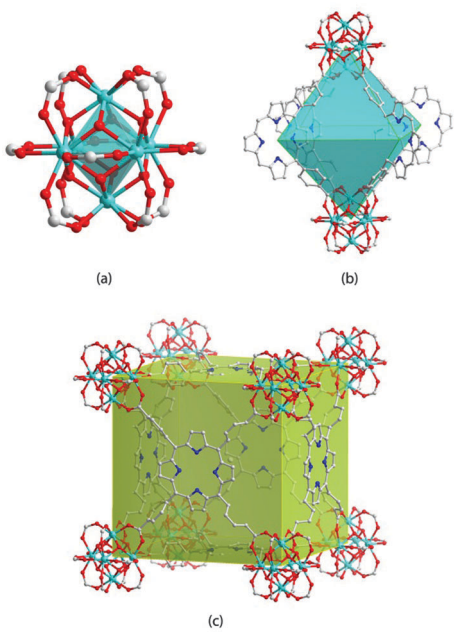


Fig. 12 (a) $Zr_6(OH)_4O_4(CO_2)_{12}$ SBU in MOF-525; (b) the octahedral cage in MOF-525 and (c) the cubic cage in MOF-525.

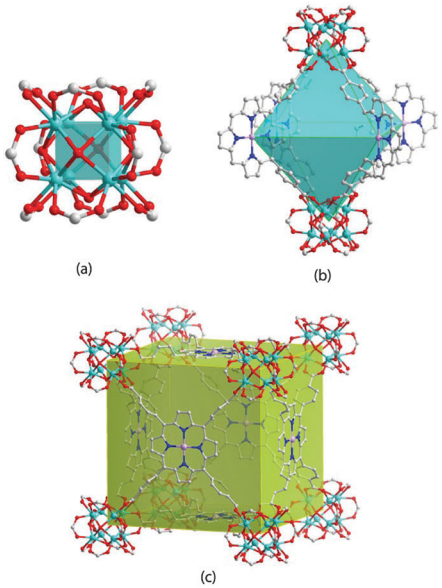


Fig. 13 (a) $Zr_8O_6(CO_2)_{12}$ SBU in PCN-221; (b) the octahedral cage in PCN-221 and (c) the cubic cage in PCN-221.

and four tcpp ligands in the equatorial plane to form a slightly distorted octahedron with a cavity diameter of ~1.1 nm (Fig. 13(b)). The other cage (Fig. 13(c)) displays a cube analogous to that of MOF-525. On the basis of the 12-connected Zr SBUs ($Zr_6O_4(OH)_4(CO_2)_{12}$/$Zr_8O_6(CO_2)_{12}$) and the 4-connected square tcpp ligand, both of these two frameworks possess an **ftw** topology and demonstrate high surface areas. Remarkably, since Zr(IV) fails to metalate the porphyrin during the synthesis of MOF-525 and PCN-221, the porphyrin remains as free-base and available for pre- and postsynthetic metalation procedures. Therefore, these polyhedron cages can be potentially functionalized by metalating a variety of metal ions into the porphyrins.

### 3.4 Postsynthetic modification

The conventional approach to MOFs synthesis largely depends on a one-pot solvothermal assembly accommodating the selected metal ion and custom-designed organic ligand under specific conditions. The development of MOFs for further applications has become increasingly reliant on the development of sophisticated MOFs endowed with complex chemical and physical functionalities. Postsynthetic modification after the initial crystallization proves an effective approach to confer more functionality on MOFs.

The dual components of organic–inorganic hybrid MOFs represent two variables of the postsynthetic modification, thus providing tunability or tailorability for both the ligand and the metal. It can be visualized that free-base porphyrinic frameworks would enable us to introduce a wide variety of metal ions *via* postsynthetic metalation to afford targeted functionality, the investigation of which is in its early infancy. This is partially caused by the fact that under MOFs synthesis conditions, the porphyrins are usually metalated spontaneously with metal ions in the solution. Rather than postsynthetic metalation to

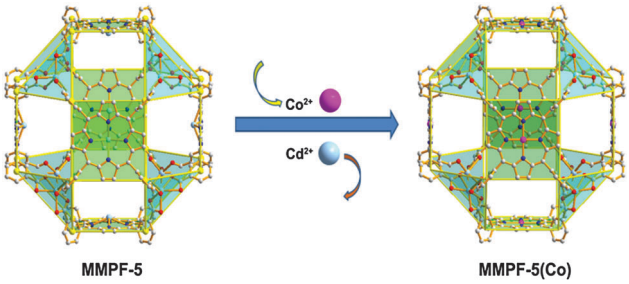


Fig. 14 Representation of metal exchange from weakly bonded Cd in MMPF-5 to strongly bonded Co in MMPF-5(Co). Reprinted (adapted) from ref. 84.

free-base porphyrins, weakly coordinated metal ions within porphyrin cores are anticipated to be exchanged by other liable metal ions by use of post-assembly chemistry. This is well illustrated by formation of a catalytically active metalloporphyrinic nanoreactor achieved by postsynthetic metal-ion exchange from Cd(II) to Co(II) of a polyhedral-cage containing MMPF, shown in Fig. 14.[84]

In terms of postsynthetic modification on organic linkers, ligand exchange so far has been only observed within the pillared MMPFs structures, in which dipyridyl pillar molecules can be replaced by other similar molecules. Choe and co-workers successfully demonstrated a single-crystal to single-crystal transformation resulting from a ligand exchange strategy in a 2D bilayer framework and a 3D pillared-layer framework.[55] By immersing the pillared porphyrinic MOFs into a solution containing dipyridyl linkers, the spontaneous pillar exchange process was observed, as shown in Fig. 15. Additionally, a pillar insertion was also observed when excess linker was used with 2D MOF structures, inducing an

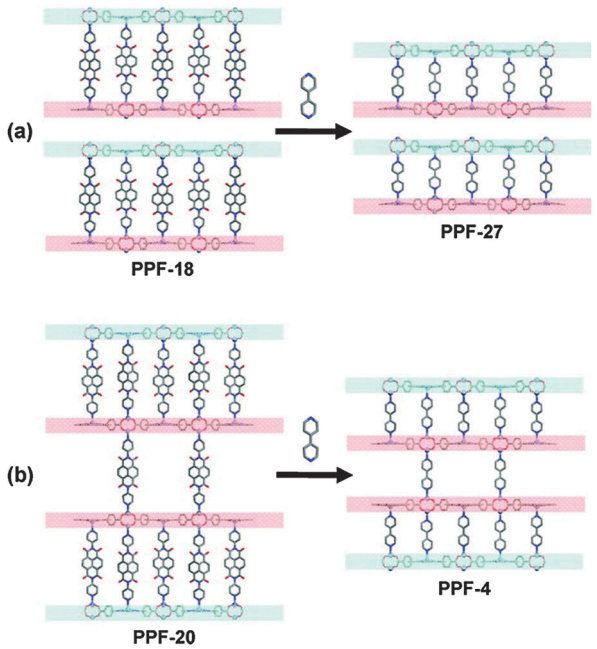


Fig. 15 Introduction of the bridging linker bipyridine to crystals of (a) PPF-18 and (b) PPF-20, transforming them to PPF-27 and PPF-4, respectively. Reprinted (adapted) with permission from ref. 55. Copyright © 2011, American Chemical Society.

overall 2D to 3D transformation. The reversible process from a 3D structure to 2D sheet was also recognized by Hupp and co-workers.[62] Furthermore, when dipyridyl metalloporphyrin struts were regarded as pillars in 3D MOFs, they were seen to be replaced by other dipyridyl porphyrin struts (free-base or other ions metalated).[66] A ligand exchange/insertion strategy engenders considerable promise for synthesizing otherwise inaccessible porphyrinic frameworks.

# 4. Applications

The applications of porphyrin-based MOFs are significantly underdeveloped compared with the large family of porphyrin-based materials. In the following discussions, we emphasize such widely investigated applications as guest molecule adsorption and separation, catalysis, nano-thin films and light-harvesting.

## 4.1 Guest molecules adsorption and separation

One of the remarkable features of MOFs lies in their high surface area and large pore volume, capable of being tuned and functionalized by crystal engineering, pillared-layer strategies, and others discussed above. Porphyrin-derived ligands add another dimension to tailor the frameworks, since porphyrin cores can incorporate a variety of metal ions. If the metalloporphyrin struts are aligned to constitute the channels or polyhedral cages, porphyrin metal centers would provide effective accessibility to different guest molecules. Therefore, this enables metalloporphyrin-based networks with great potential as functional porous materials for guest molecules adsorption and separation.

In terms of porosity, adsorption and separation studies, internal surface area plays a primary role in evaluating the behavior of porous materials. In order to provide an overview of porosity studies of porphyrin-based MOFs, we summarize all the reported surface area values of porphyrin-derived MOFs from the literature in Table 1. Although many efforts have been devoted to building-up open porphyrin-based architectures since the 1990s, examples of materials stable upon solvent removal and displaying permanent porosities detected by gas adsorption still remain scarce.

Initial studies of functional microporous behavior were prompted by mimicking inorganic zeolite paradigms, as previously discussed PIZA-1 exhibits size-, shape- and functional group-selective sorption behavior for a series of solvent guest molecules (Fig. 16).[43] More specifically, the channeled PIZA-1 has a calculated accessible void volume of 47.9%, which is significantly larger than that of Zeolite 4A, the molecular sieve, at the value of 27.2% (on the basis of a 1.4 Å probe radius). The selective sorption was conducted by exposing desolvated PIZA-1 to different guest solvents while being monitored by gravimetric thermal desorption. PIZA-1 demonstrated an extremely high capacity for repeated rapid adsorption of water, which is incomparable to Zeolite 4A and $ALPO_4$-18 molecule sieves. PIZA-1 retains its structural integrity after ten adsorption–desorption cycles. Further investigation showed PIZA-1's ability to perform size- and shape-selective sorption for less sterically hindered and more polar compounds with regard to a series of linear amines, aromatic amines, picoline derivatives, and alcohols, respectively, by comparing the uptake capacity toward different guest molecules. PIZA-1 also possesses extraordinary properties as a desiccant for the selective drying of common organic solvents (for example, benzene, toluene and tetrahydrofuran), when compared with Zeolite 4A. These selective adsorption behaviors can be mainly illustrated by the hydrophilic nature of the channels and the limited pore size.

While PIZA-1 shows interesting selective sorption behavior to a wide range of guest molecules, it is still considerably limited by its relatively low surface area (BET surface area at 125 $m^2\ g^{-1}$ probed by nitrogen adsorption isotherm). It is thus still highly desirable to build up porphyrin-based frameworks featuring high surface area.

MOFs have attracted plenty of attention over the past two decades due to their great potential for a plethora of applications, especially in the field of gas storage and separation. Porous porphyrin-derived MOFs also have been assessed by their gas uptake capacity and separation ability. For instance, PPF-1,[49] $Zn_2$(Zn-TCPP)·$3H_2O$·2DMF, features a two dimensional square grid network, assembled from $Zn(CO_2)_4$ paddlewheel units and tetratopic TCPP ligands. The permanent microporosity of PPF-1 was confirmed by a type-I nitrogen ($N_2$) sorption isotherm at 77 K with a surface area of 622.4 $m^2\ g^{-1}$. A hydrogen ($H_2$) adsorption test was also performed on the porous PPF-1, which shows a reversible uptake of 1.0 wt% (10.3 mg $g^{-1}$) at 1 bar and 77 K. The high-pressure $H_2$ uptake capacity is up to 2.0 wt% at 20 bar and 77 K, corresponding to 9.8 $H_2$ molecules per formula unit. The very moderate capacity value of PPF-1 is largely restricted by its low surface area and weak interaction between $H_2$ molecules and frameworks.

Another example investigates how the extra-framework cations ($Li^+$, $Na^+$, $K^+$, $Rb^+$ and $Cs^+$) tune the $O_2/N_2$ separation behaviors of a porous porphyrin-derived framework.[108] The porphyrin-derived network (labeled as MIL-141) was determined as a 3-fold interpenetrating **pts**-topology structure, constructed by iron(III) with the nickel-metalated TCPP ligand, shown in Fig. 17. The judiciously selected iron(III) attempts to build a stable porphyrinic framework, as it is established that the highly charged cations ($M^{3+}$ = $Al^{3+}$, $Cr^{3+}$, $Fe^{3+}$; $M^{4+}$ = $Ti^{4+}$, $Zr^{4+}$) derived solids are often more stable than those based on $M^{2+}$ cations (especially $M^{2+}$ = $Cu^{2+}$, $Zn^{2+}$, $Cd^{2+}$). The series of these anionic porphyrin-derived networks charge-balanced by alkali cations (trapped in pores) shows stability upon solvent removal and possess a significant permanent porosity. The cations/framework affinities are stronger in MIL-141 than those in analogous cation-containing zeolites resulting in a lower $N_2$/framework interaction and thus a reverse $N_2$ over $O_2$ selectivity (Fig. 18). Moreover, this demonstrates that the metalloporphyrin ligands preferentially adsorb $O_2$ over $N_2$, which is further supported by the natural role of porphyrin for $O_2$ transportation.

The selective adsorption phenomenon is also observed in MMPF-1, the first example of a MOP-based porphyrinic framework.[78] The "ABAB" packing of the irregular rhombicuboctahedral

 

Table 1 Reported surface area values of porphyrin-derived MOFs

| Common name | Chemical formula (guest molecule ignored) | Surface area/$m^2$ $g^{-1}$ BET | Langmuir | Year | Author (ref.#) |
|---|---|---|---|---|---|
| PIZA-1 | $[CoT(p\text{-}CO_2)PPCo_{1.5}]$ | 125 | NA | 2002 | Suslick[43] |
| PIZA-4 | $[Zn(p\text{-}CO_2)P_2Mes_2P]_3Zn_4O$ | NA | 800 | 2003 | Suslick[44] |
| $[Cu_2(AcO)_4(CuTPyP)_{1/2}]$ | $[Cu_2(AcO)_4(Cu\text{-}tpyp)_{1/2}]$ | 812.08 | 1035.96 | 2006 | Ohmura[107] |
| PPF-1 | $[Zn_2(Zn\text{-}tcpp)]$ | NA | 622.4 | 2009 | Choe[49] |
| ZnPO-MOF | $[Zn_2(\mathbf{1})(Zn\text{-}\mathbf{2})]$<br>**1** = 1,2,4,5-tetrakis(4-carboxyphenyl)benzene<br>**2** = (5,15-dipyridyl-10,20-bis(pentafluorophenyl))porphyrin | NA | 500 | 2009 | Hupp[60] |
| ZnMn-RPM | $Zn_2(L^1)(L^2)$<br>$L^1$ = Zn-tcpp<br>$L^2$ = (5,15-dipyridyl-10,20-bis(pentafluorophenyl))porphyrinMnCl | NA | 1000 | 2011 | Hupp[61] |
| BOP | $Zn_2(Zn\text{-}L^2)(L^3)$<br>$L^2$ = tcpp<br>$L^3$ = boron dipyrromethene (bodipy) | NA | 540 | 2011 | Hupp[62] |
| MIL-141(A) | Fe(Ni-tcpp)A<br>A = Li, Na, K, Rb, Cs | 635 (Li)<br>510 (Na)<br>810 (K)<br>820 (Rb)<br>860 (Cs) | NA | 2011 | Devic[108] |
| $Zn_4$·ZnTCPEP·DABCO | $Zn_4\text{-}(\mu_3\text{-}OH)_2(H_2O)_2(Zn\text{-}tcpep\text{-}H)_2$ (DABCO) | 461 | 581 | 2011 | Matsunaga[98] |
| MMPF-1 | $Cu_2(Cu\text{-}bdcpp)(H_2O)_2$ | NA | 420 | 2011 | Ma[78] |
| MMPF-2 | $[Co(II)_3(OH)(H_2O)]_4(Co(II)tdcpp)_3$ | 1410 | 2037 | 2012 | Ma[82] |
| MMPF-3 | $[Co_2(\mu_2\text{-}H_2O)(H_2O)_4](Co\text{-}dcdbp)$ | NA | 750 | 2012 | Ma[80] |
| MMPF-4 | $[Zn_{19}(tdcpp)_3][(NO_3)_8]$ | 958 | 1205 | 2012 | Ma[81] |
| MMPF-5 | $[Cd_8(Cd\text{-}tdcpp)_3][(H_3O)_8]$ | NA | 740 | 2012 | Ma[81] |
| Al-PMOF | $H_2tcpp[AlOH]_2$ | 1400 | NA | 2012 | Rosseinsky[109] |
| Al/Zn-PMOF | $Zn_{0.986}\text{-}tcpp[AlOH]_2$ | 1200 | | | |
| $[Cu_2(MDDCPP)]$ | $[Cu_2(M\text{-}ddcpp)]$<br>M = $Zn^{2+}$, $Ni^{2+}$, $Pd^{2+}$, $Mn^{3+}$ ($NO_3$), $Ru^{2+}(CO)$ | 498 (Zn)<br>647 (Ni)<br>379 (Pd)<br>509 (Mn)<br>819 (Ru(CO)) | 613 (Zn)<br>864 (Ni)<br>486 (Pd)<br>680 (Mn)<br>968 (Ru(CO)) | 2012 | Matsunaga[110] |
| MOF-525 | $Zr_6O_4(OH)_4(tcpp\text{-}H_2)_3$ | 2620 | NA | 2012 | Yaghi[106] |
| MOF-545 | $Zr_6O_8(H_2O)_8(tcpp\text{-}H_2)_2$ | 2260 | NA | 2012 | Yaghi[106] |
| PCN-222 (Fe) (isostructural MOF-545) | $Zr_6O_8(H_2O)_8(FeCl\text{-}tcpp)_2$ | 2200 | NA | 2012 | Zhou[67] |
| MMPF-6 (isostructural MOF-545) | $Zr_6O_8(H_2O)_8(FeCl\text{-}tcpp)_2$ | 2100 | NA | 2012 | Ma[79] |
| MMPF-5 (Co) | $[Cd_8(Co\text{-}tdcpp)_3][(H_3O)_8]$ | NA | 600 | 2013 | Ma[84] |
| MMPF-7 | $[In_{1.29}O_{0.57}$ (tcpp)] | NA | 600 | 2013 | Ma[83] |
| MMPF-8 | [In(In-tcbpp)] | 440 | 510 | 2013 | Ma[83] |
| MMPF-9 | $Cu_6(Cu\text{-}tdcbpp)(HCO_2)_4(H_2O)_6$ | 850 | 1050 | 2014 | Ma[85] |
| CZJ-1 | $Zn_2(MnOH\text{-}tcpp)(DPNI)$<br>DPNI = *N*,*N*′-di-(4-pyridyl)-1,4,5,8-naphthalenetetracarboxydiimide | NA | 500 | 2013 | Chen and Wu[77] |
| Zr–PCN-221(no metal) | $Zr_8O_6(tcpp)_3$ | 1963 | NA | 2013 | Zhou[69] |
| Zr–PCN-221(Fe) | $Zr_8O_6(FeCl\text{-}tcpp)_3$ | 1549 | | | |
| Hf–PCN-221(Co) | $Hf_8O_6(Co\text{-}tcpp)_3$ | 1532 | | | |
| PCN-224 | $(Zr_6O_{20})_2(Ni\text{-}tcpp)_3$ | 2600 | NA | 2013 | Zhou[68] |
| PCN-225 | $Zr_6(\mu_3\text{-}O)_4(\mu_3\text{-}OH)_4(OH)_4(H_2O)_4(H_2\ tcpp)_2$ | 1902 | 2080 | 2013 | Zhou[70] |

cages leads to the tiny pore size of MMPF-1, prompting the evaluation of its performance as a selective gas adsorbent. As indicated by a series of gas adsorption tests on the activated sample (Fig. 19), MMPF-1 only adsorbs a very limited amount of $N_2$ (5 $cm^3$ $g^{-1}$) at 77 K and ~760 Torr. In contrast, a larger amount of $H_2$ uptake (50 $cm^3$ $g^{-1}$) is observed under the same conditions. A substantial uptake of 45 $cm^3$ $g^{-1}$ is also found for $O_2$ at its saturation pressure of 154 Torr at 77 K. Gas adsorption studies at 195 K indicated that MMPF-1 can take up a large amount of $CO_2$ (80 $cm^3$ $g^{-1}$) at 760 Torr, which is much higher than the amount of $CH_4$ (18 $cm^3$ $g^{-1}$). The interesting molecular sieving effect observed for MMPF-1 is attributed to its small aperture size of ~3.5 Å, which excludes larger gas molecules of $N_2$ and $CH_4$ with kinetic diameters of 3.64 and 3.8 Å, respectively, but allows the entry of smaller gas molecules of $H_2$ (kinetic diameter 2.89 Å), $O_2$ (kinetic diameter 3.46 Å), and $CO_2$ (kinetic diameter 3.3 Å). MMPF-1 presents unusual adsorption behavior, selectively adsorbing $H_2$ and $O_2$ over $N_2$, and $CO_2$ over $CH_4$.

Molecular porphyrins used as appealing MBBs expand the possibilities of modular design by virtue of incorporating versatile metal ions into porphyrin cores. The porphyrin centers of MMPF-1 were metalated *in situ* by Cu(II) ions in the same way as those in the paddlewheel SBUs during the course of assembly. Matsunaga *et al.* premetalated the porphyrin ligand with $Zn^{2+}$,

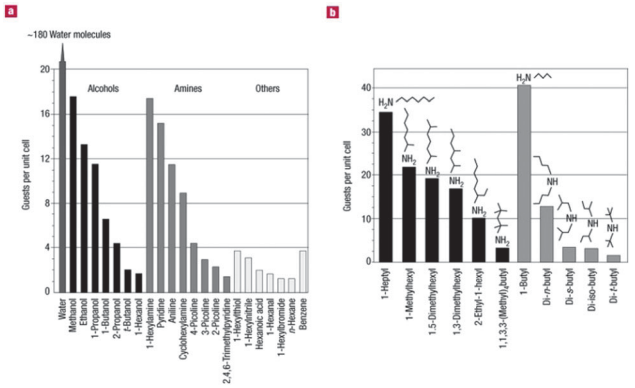


Fig. 16 Size-, shape-, and functional-group selectivity of PIZA-1 as probed by thermal desorption of guest molecules. Reprinted (adapted) with permission from ref. 43. Copyright © 2002, Rights Managed by Nature Publishing Group.

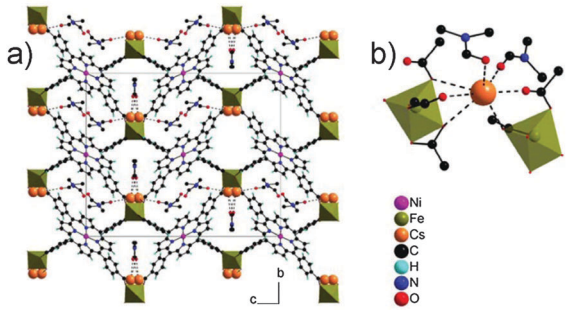


Fig. 17 (a) View of MIL-141(Cs) along [100]; for the sake of clarity, two channels (top right) are depicted without the DMF molecules. (b) Coordination sphere of the Cs+ cation; both Cs+ and DMF molecules present a positional disorder, only one position is depicted. Reprinted (adapted) with permission from ref. 108. Copyright © 2011, American Chemical Society.

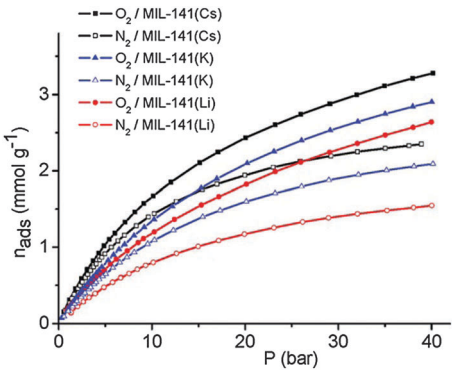


Fig. 18 Nitrogen and oxygen sorption isotherms measured at 303 K for MIL-141(A) (A = Li, K, Cs). Reprinted (adapted) with permission from ref. 108. Copyright © 2011, American Chemical Society.

$Ni^{2+}$, $Pd^{2+}$, $Mn^{3+}$ and $Ru^{2+}$, and constructed a series of isostructural frameworks without alteration of the MMPF-1 topology net.[110] Tetrahydrofuran was examined as an effective activating solvent improving $N_2$ uptake capacity compared to those exchanged by dichloromethane or methanol. $N_2$ adsorption isotherms at 77 K demonstrated BET surface areas of 498 $m^2\ g^{-1}$, 647 $m^2\ g^{-1}$, 379 $m^2\ g^{-1}$, 509 $m^2\ g^{-1}$, and 810 $m^2\ g^{-1}$ for $[Cu_2(ZnDDCPP)]$, $[Cu_2(NiDDCPP)]$, $[Cu_2(PdDDCPP)]$, $[Cu_2(MnDDCPP)(NO_3)]$, and $[Cu_2(Ru(CO)DDCPP)]$, respectively. Additionally, DMF guest molecules confined in the cavity cannot be removed completely due to the small pore window. The different surface areas of the series structures were attributed mainly to the number of residual DMF guest molecules in the cage. The work presented demonstrates the ability to modulate porphyrin linkers with a variety of metal ions, generating a tool to functionalize the frameworks with accessible metal sites.

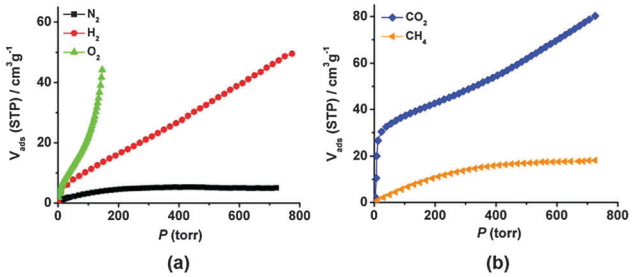


Fig. 19 Gas adsorption isotherms of MMPF-1 at (a) 77 K and (b) 195 K. Reprinted (adapted) with permission from ref. 78. Copyright © 2011, American Chemical Society.

$CO_2$, a major greenhouse gas, has accumulated in the atmosphere at an alarming pace and this has prompted the development of efficient porous materials for $CO_2$ capture. In our quest for the discovery of porous porphyrin-derived frameworks focusing specifically on $CO_2$ capture and storage, a highly porous porphyrin-based network, labeled as MMPF-2,[82] was constructed from a custom-designed octatopic ligand, tetrakis-(3,5-dicarboxyphenyl)porphyrine ($H_{10}$tdcpp) and a robust distorted cobalt trigonal prism SBU generated *in situ*. The tdcpp ligand featuring the mono-chelated carboxylate groups was revealed to bridge rigidly two other tdcpp ligands *via* eight distorted trigonal prism SBUs, resulting in porphyrin macrocycles located in a "face to face" configuration with a distance between porphyrin rings of 10.262 Å (Fig. 20). The porphyrin cores of the ligands were metalated *in situ* by cobalt(II) during the synthetic process of MMPF-2. The cobalt ions within the porphyrin macrocycles provide accessible sites toward the channels from the distal and proximal positions, allowing guest molecules to bind.

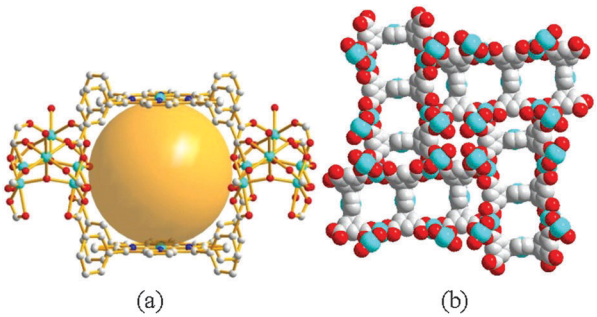


Fig. 20 (a) Three cobalt porphyrins located in the "face-to-face" configuration in MMPF-2; (b) space filling model of three types of channels in MMPF-2 viewed from the *c* direction. Reprinted (adapted) from ref. 82.

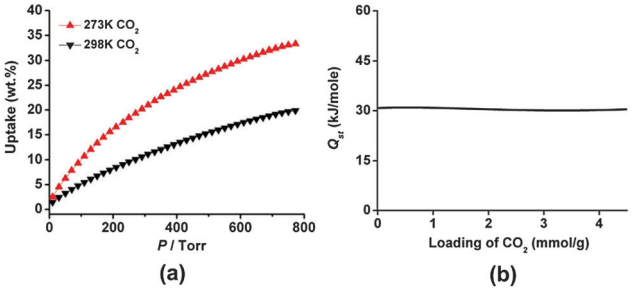


Fig. 21 (a) $CO_2$ adsorption isotherms of MMPF-2 at 273 K and 298 K; (b) isosteric heats of adsorption of MMPF-2 for $CO_2$. Reprinted (adapted) from ref. 82.

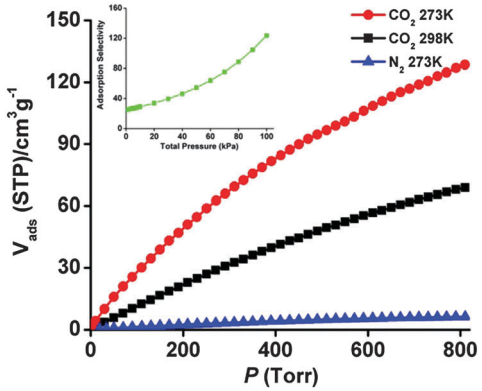


Fig. 22 $CO_2$ adsorption isotherms at 273 K (red) and 298 K (black), $N_2$ adsorption isotherm (blue) at 273 K, and IAST-predicted adsorption selectivity (inset green) for MMPF-4 at 273 K. Reprinted (adapted) from ref. 81.

Derived from the Ar adsorption isotherm at 87 K, MMPF-2 was reported to possess a Langmuir surface area of 2037 $m^2\ g^{-1}$ upon the removal of guest solvent molecules. The measured pore volume of MMPF-2 is 0.61 $cm^3\ g^{-1}$, which matches the calculated value of 0.63 $cm^3\ g^{-1}$, highlighting the robustness of its framework. The $CO_2$ uptake performances were also investigated on MMPF-2 (Fig. 21). MMPF-2 shows an uptake capacity of 33.4 wt% (or 170 $cm^3\ g^{-1}$) at 273 K and 760 Torr, which is comparable to the highest value of 38.5 wt% for SNU-5 under the same condition in spite of its much lower surface area (2037 $m^2\ g^{-1}$ *vs.* 2850 $m^2\ g^{-1}$). Accordingly, this value is the highest $CO_2$ uptake capacity among all the porous porphyrin/metalloporphyrin-based frameworks under the same conditions. The $CO_2$ uptake capacity of MMPF-2 at 298 K and 760 Torr is 19.8 wt% (or 101 $cm^3\ g^{-1}$), which is also among the highest values for porous MOFs under the same conditions. Calculated from adsorption isotherms at 273 K and 298 K, a constant heats of adsorption ($Q_{st}$) value of ~31 kJ $mol^{-1}$ was established over the loading range for MMPF-2. This is distinctive compared with other MOFs with open metal sites, whose $Q_{st}$ usually decreases drastically to 20–25 kJ $mol^{-1}$ with the increase of $CO_2$ loading despite their high initial value. This is ascribed tentatively to the high density of open metal sites (~5 open cobalt sites $nm^{-3}$) toward the channels in MMPF-2.

$CO_2$ adsorption studies were also performed on MMPF-7 and MMPF-8, indium-based porous **pts**-topology MMPFs.[83] These two networks were constructed by self-assembly of In(III) with tcpp or 5,10,15,20-tetrakis(4-carboxybiphenyl)-porphyrin (tcbpp) ligand, respectively. The In(III) ions serve as 4-connected tetragonal nodes and the tetracarboxyporphyrin ligands as 4-connected planar nodes, resulting in a **pts**-topology net. MMPF-7 demonstrates three-fold interpenetration due to the strong π–π interactions among the porphyrin macrocycles. However, the extension from tcpp to tcbpp *via* the phenyl ring leads to a four-fold interpenetrating 3D structure in MMPF-8. MMPF-7 adsorbs a substantial amount of $CO_2$ with an uptake of 10.7 wt% (55 $cm^3\ g^{-1}$) at 273 K and 6.6 wt% (34 $cm^3\ g^{-1}$) at 298 K under 760 Torr. In comparison, MMPF-8, with a higher degree of interpenetration, demonstrates an enhanced $CO_2$ uptake capacity of 16.2 wt% (82 $cm^3\ g^{-1}$) at 273 K and 9.3 wt% (47 $cm^3\ g^{-1}$) at 298 K under 1 atm. The higher $CO_2$ uptake is presumably ascribed to its larger surface area when compared to MMPF-7 (910 $m^2\ g^{-1}$ *vs.* 600 $m^2\ g^{-1}$ calculated by non-local density functional theory on the basis of $CO_2$ adsorption isotherms at 273 K), since the calculated $Q_{st}$ of $CO_2$ of MMPF-8 is lower than that of MMPF-7 (~28 kJ $mol^{-1}$ *vs.* ~32 kJ $mol^{-1}$).

MMPF-4 and MMPF-5 also exhibit permanent porosities.[81] It is noteworthy that MMPF-4 demonstrates interesting selective adsorption of $CO_2$ over $N_2$. The $CO_2$ adsorption isotherms indicate that MMPF-4 can take up an amount of 24.4 wt% (124 $cm^3\ g^{-1}$) at 273 K and 13.4 wt% (67 $cm^3\ g^{-1}$) at 298 K under 1 atm pressure, as shown in Fig. 22. Furthermore, the potential of MMPF-4 for possible combustion $CO_2$ capture application is also assessed by calculating adsorption selectivity from pure-component ($CO_2$, $N_2$) adsorption isotherms at the same temperature. The ideal adsorption solution theory (IAST) is employed to estimate the selectivity of MMPF-4 for $CO_2/N_2$ in postcombustion flue gas streams typically composed of 15% $CO_2$ and 85% $N_2$. MMPF-4 is calculated to exhibit an adsorption of selectivity of 123 for $CO_2$ over $N_2$ at 273 K and 1 bar.

In the foregoing discussion, selective sorption of solvent guest molecules, gas adsorption and selective adsorption are studied widely among the porous porphyrin/metalloporphyrin-based frameworks. However, there still remains a desire to develop metalloporphyrin-based networks exhibiting permanent porosity upon the removal of solvent guests, higher surface areas, larger pore volumes, and functionalizable pore surfaces. To meet these demands, a series of highly stable porphyrin-based frameworks have been constructed derived from the highly charged cations of $Zr^{4+}/Hf^{4+}$.[67–69,79,106] The free-base porphyrin of the ligands can be pre- or post-metalated by a wide range of available metal ions to functionalize the frameworks. In fact, among all porphyrin-based MOFs, the highest surface area value belongs to MOF-525 (~2620 $m^2\ g^{-1}$), a polyhedral network.[106] Other frameworks such as MOF-545/PCN-222/MMPF-6 (isostructures), PCN-221 and PCN-224 also display a relatively high surface area (shown in Table 1), providing readily functionalizable platforms for other applications.

### 4.2 Catalysis

On account of the structural similarity to cofactors found in many metallo-enzymes, extensive research has looked to exploit metalloporphyrin units to mimic the facile natural catalytic cycles. Additionally, organometallic chemistry demonstrates metalloporphyrins as homogeneous catalysts possessing high catalytic activity towards the hydroxylation of alkanes and epoxidation of alkenes. The rational design and synthesis of expanded porous metalloporphyrin networks incorporating catalytically active metalloporphyrins as struts have the potential to act as size- and shape-selective heterogeneous catalysts within well-defined structures. Moreover, the ability to separate and recycle the heterogeneous catalysts would be very attractive in large-scale reactions, where separation and waste disposal can be costly.

Depending on the mechanistic process, the catalytic reactions can be divided into several types of reactions, including oxidation catalysis, Lewis acid catalysis, photocatalysis, biomimetic catalysis and electrocatalysis. The following discussion examines systematically effective strategies to build up catalytically active metalloporphyrin frameworks.

**4.2.1 Oxidation catalysis.** The first reported metalloporphyrin-based framework showing catalytic activity, PIZA-3, was published in 2005.[45] PIZA-3 demonstrates heterogeneous catalytic oxidation of a variety of linear and cyclic alkanes and epoxidation of cyclic alkenes. Unfortunately, the constrained microporous channels restrict the catalytic process, allowing it to occur on the exterior of the framework, rather than the interior, resulting in no size- and shape-selectivity towards substrates. Thus, constructing metalloporphyrin-based frameworks as heterogeneous catalysts for size- and shape-selective oxidation reactions remains a challenge.

Despite extensive prior synthesis efforts, ZnMn-RPM was the first metalloporphyrin-based MOF to exhibit oxidation catalytic activity on the interior surface of the material.[61] A variety of metalloporphyrins (especially, $Al^{3+}$, $Zn^{2+}$, $Pd^{2+}$, $Mn^{3+}$ and $Fe^{3+}$ complexes) were incorporated directly into a family of porphyrin-based MOFs (Fig. 23). These robust porphyrinic materials (RPMs) feature pillared-layer structures, demonstrate large channels and permanent porosity with a surface area of $\sim$1000 $m^2$ $g^{-1}$. The readily accessible active sites decorate on the channel surface, inducing ZnMn-RPM with catalytic activity for the oxidation of alkenes and alkanes. The styrene epoxidation reaction was examined using 2-(*tert*-butylsulfonyl)iodosylbenzene as oxidant with homogeneous 5,10,15,20-tetrakis(pentafluorophenyl)-porphyrin Mn(Cl) as control to compare with the heterogeneous ZnMn-RPM. The homogeneous Mn complex showed complete deactivation after 780 epoxidation turnovers, due to the formation of an oxo-bridged dimer. However, the heterogeneous ZnMn-RPM functioned until depletion of the oxidant in 2150 turnovers. These results demonstrate an advantage heterogeneous metalloporphyrin frameworks possess over their homogeneous component. ZnMn-RPM was also an effective catalyst for oxidation of cyclohexane in the yield of 20% to cyclohexanol and cyclohexanone (83 : 17).

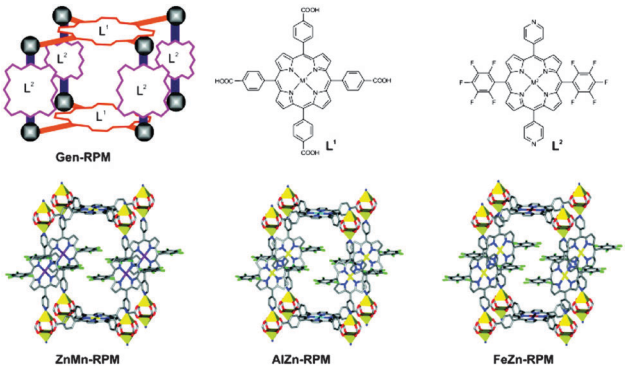


Fig. 23 Structure of RPM materials. Top left: a schematic representation of a generic RPM unit cell. Top center and right: structures of the porphyrinic struts used to synthesize the RPM series ($M^1$ = 2H, Pd, Al(OH) or Fe(Cl), $M^2$ = 2H or Mn(Cl)); bottom: crystallography-derived stick representations of the unit cells of three representative RPMs. Reprinted (adapted) with permission from ref. 61. Copyright © 2011, American Chemical Society.

MMPF-3,[80] using **fcu**-MOF-1 as the blueprint, was engineered to be an **fcu**-topology polyhedral cage-based framework. The high density of cobalt metal centers in the truncated octahedral cages prompted evaluation of its catalytic performance in the epoxidation of *trans*-stilbene. *tert*-Butyl hydroperoxide (tbhp) was used as oxidant for the catalytic reactions, carried out with MMPF-3, the homogeneous cobalt-metalated porphyrin, **fcu**-MOF-1 and other controls (Fig. 24). The high catalytic activity of MMPF-3 was attributed tentatively to the high density of cobalt centers oriented directly towards the channel centers. Moreover, upon removal of MMPF-3, no detectable leaching of active site or cobalt ion in the reaction solution occurred, and MMPF-3 maintained its catalytic activity for eight cycles. These results highlight how appropriately designed polyhedral cages can serve as efficient nanoreactors for catalytic reactions.

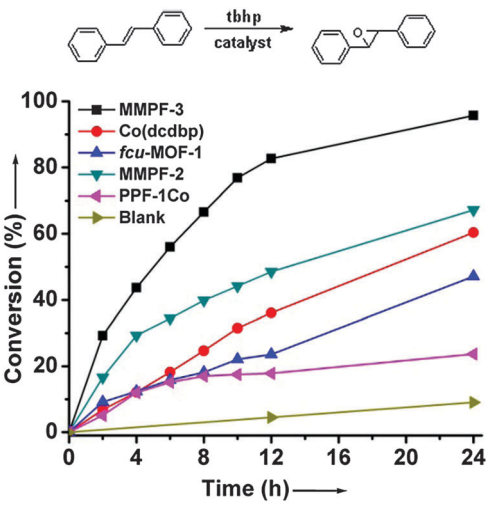


Fig. 24 Kinetic traces of *trans*-stilbene epoxidation catalyzed by heterogeneous MMPF-3, homogenous Co(dcdbp), **fcu**-MOF-1, PPF-1Co, and in the absence of catalyst. Reprinted (adapted) with permission from ref. 80. Copyright © 2012 WILEY-VCH Verlag GmbH & Co. KGaA, Weinheim.

Table 2 Summary of catalytic data for epoxidation of *trans*-stilbene catalyzed by MMPF-5(Co) and related catalysts. [a] Reprinted (adapted) from ref. 84

| Catalyst | Conversion[b] (%) | Epoxide (%) |
|---|---|---|
| MMPF-5(Co) | 87.0 | 81.5 |
| tdcmpp(Co)[b] | 28.1 | 64.4 |
| MMPF-5 | 9.2 | 55.1 |
| Blank | 9.0 | 55.8 |
| Filtrate[c] | 9.1 | 55.9 |
| MMPF-5(Co)[d] | 80.1 | 80.2 |

[a] *trans*-Stilbene (1 mmol), *t*BuOOH (3.0 mmol), catalyst (0.001 mmol), acetonitrile (5.0 mL) were stirred at 608 °C for 24 h. [b] 0.003 mmol catalyst. [c] After catalytic assay for MMPF-5(Co). [d] The fifth cycle.

Following MMPF-3, Ma and co-workers reported another facile route to create metalloporphyrin-based nanoreactors *via* post-synthetic metal ion exchange, replacing inactive Cd(II) metal cations with catalytically active Co(II).[84] The free-base porphyrin ligand (tdcpp) was metalated *in situ* by Cd(II) during the assembly of nanoscopic small cubicuboctahedral cages of the parent MMPF-5. The Cd(II) cation residing within the porphyrin ring lies far out of the porphyrin plane, which provides an opportunity to be exchanged by smaller divalent metal cations. The complete exchange of Cd(II) cations with Co(II) within the porphyrin cores of tdcpp ligands results in the framework of MMPF-5(Co). In the context of epoxidation of *trans*-stilbene, MMPF-5(Co) demonstrated improved yield and selectivity compared to the parent MMPF-5 or the homogeneous cobalt-based porphyrin ligand (Table 2). As illustrated above, post-synthetic metal ion exchange enables the catalytically inactive framework to become a highly active catalyst for the epoxidation of *trans*-stilbene. Additionally, the single crystallinity and permanent porosity are also preserved during the course of metal exchange.

Wu and co-workers demonstrated a series of highly efficient metalloporphyrin-based MOF catalysts for the oxidation of alkylbenzenes. The initial work constructed an organic–inorganic hybrid layered structure based on Mn(III)–porphyrin and polyoxometalate (POM), as illustrated in Fig. 25.[76] The hybrid solid features a catalytically active Mn(III)–porphyrin species, and thus performs selective oxidation of ethylbenzene to acetophenone

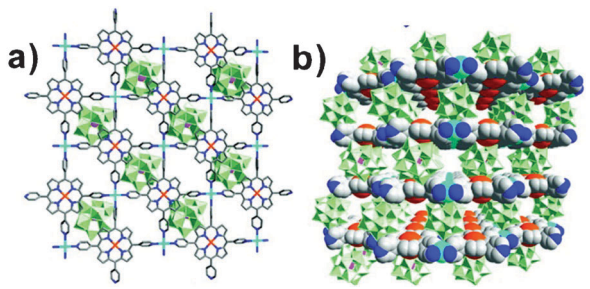


Fig. 25 (a) Arrangement of a single layer of the lamellar framework of $[Cd(DMF)_2Mn^{III}(DMF)_2TPyP]_n^{3n+}$ and a layer of the $[PW_{12}O_{40}]^{3-}$ polyanions, as viewed down the *c*-axis. (b) Perspective view of the packing diagram along the [110] direction. Reprinted (adapted) with permission from ref. 76. Copyright © 2012, American Chemical Society.

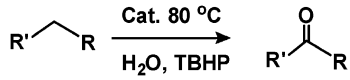


Scheme 2 Oxidation reaction of alkylbenzenes. Reprinted (adapted) with permission from ref. 76. Copyright © 2012, American Chemical Society.

using TBHP as oxidant (Scheme 2), as well as size- and shape-selectivity observed for a broad family of different alkylbenzenes. The robust layered framework of the Mn(III)–porphyrin units isolated by POM, preventing the formation of degraded dimers, leads to the decent stability and recyclability of the heterogeneous catalyst.

Rather than using commercially available tetrapyridylporphyrin, Wu and co-workers then used the synthetic pre-metalated tdcpp ligands (Mn/Ni-tdcpp) combined with Mn(II) or Cd(II) ions to generate three **tbo**-topology isostructural networks: ZJU-18 (in the formula of $[Mn_5Cl_2(MnCl\text{-}tdcpp)]$); ZJU-19 ($[Mn_5Cl_2(Ni\text{-}tdcpp)]$); and ZJU-20 ($[Cd_5Cl_2(MnCl\text{-}tdcpp)]$).[73] Their catalytic behaviors for the oxidation of alkylbenzenes were assessed with tbhp as the oxidant. The immobilization of Mn(III)–porphyrin active sites on the pore surface of ZJU-18 exhibits highly efficient and selective oxidation of ethylbenzene to acetophenone in the yield of >99% with a turnover number of 8076 after 48 hours. The results clearly indicate that the catalytic activity of ZJU-18 exceeds the activity of ZJU-19, ZJU-20 and the homogeneous MnCl-based porphyrin counterpart.

Zhou and co-workers further explored the catalytic oxidation of cyclohexane using metalloporphyrin derived frameworks with the development of Zr–PCN-221 (Fe).[69] The reaction proceeds very quickly and the products are obtained in an almost stoichiometric amount with about 100% consumption of used tbhp (oxidant) (Fig. 26). The framework also induces high selectivity between cyclohexanone (in the yield of 86.9%) and cyclohexanol (5.4%). The results can be attributed to the high density of accessible Fe(III) centers residing on the pore surfaces of Zr–PCN-221 (Fe). Interestingly, free-base Zr–PCN-221 demonstrates no catalytic activity towards the reaction.

Wu and co-workers studied the practicality of employing a two-fold interpenetrating pillared-layer framework, CZJ-1, as a selective oxidation catalyst for cyclohexane using iodisylbenzene

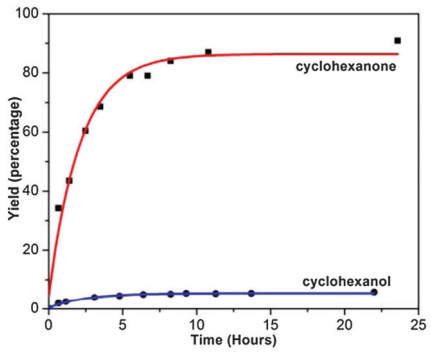


Fig. 26 Catalytic oxidation of cyclohexane over Zr–PCN-221(Fe) at 65 °C. The yields are calculated on the basis of tbhp. Reprinted (adapted) with permission from ref. 69. Copyright © 2013, American Chemical Society.

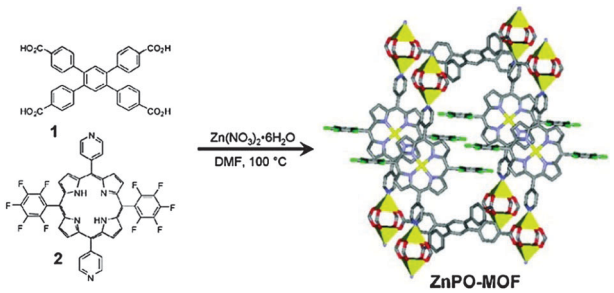


Fig. 27 Synthesis of pillared-layer ZnPO-MOF. Reprinted (adapted) with permission from ref. 60. Copyright © 2009, American Chemical Society.

as the oxidant.[77] The $Zn_2(COO)_4$ paddlewheel SBUs are bridged by Mn-tcpp forming 2D sheets that are further pillared by *N*,*N*′-di-(4-pyridyl)-1,4,5,8-naphthalenetetracarboxydiimide (dpni) to generate ultimately the 3D porous structure. CJZ-1 was also characterized as an efficient recyclable catalyst for the oxidation of cyclohexane with conversion up to 94% and about 100% selectivity toward cyclohexanone over cyclohexanol.

**4.2.2 Lewis acid catalysis.** Lewis acid catalysis mainly takes advantage of unsaturated metal sites capable of acting as electron pair acceptors and accelerating the reaction process. ZnPO-MOF,[60] a robust framework established on the pillared-layer strategy, features large pores with a surface area of $\sim$500 $m^2$ $g^{-1}$. The dipyridylporphyrin pillar is metalated *in situ* with Zn(II), with its distal and proximal directions remaining unoccupied (Fig. 27). The accessible Zn(II) centers incorporated into open channels demonstrate catalytic activity for acyl-transfer reaction between *N*-acetylimidazole and 3-pyridylcarbinol (Fig. 28). A 2420-fold rate enhancement relative to the uncatalyzed reaction is observed. The catalytic activity is ascribed tentatively to the Lewis acidic Zn(II) centers providing coordination sites to substrates and allowing pre-concentration of reactant molecules, and increasing reaction rate within the robust MOF channels.

The ring-opening of styrene epoxide with trimethylsilylazide ($TMSN_3$) represents another type of reaction catalyzed by Lewis acid, with stronger acids being more efficient catalysts.[66] The efficient catalyst, ZnAl-RPM, was introduced by solvent-assisted

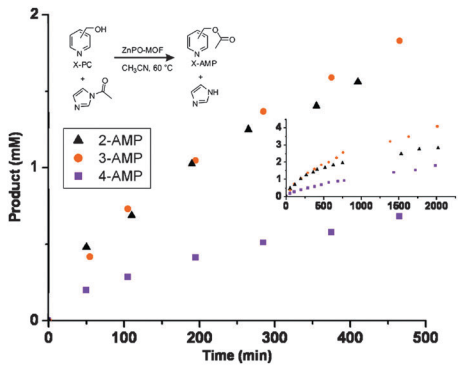


Fig. 28 Plot of product concentrations *vs.* time, showing the initial production of the various isomers of acetoxymethylpyridine (AMP) from *N*-acetylimidazole and pyridylcarbinols. Reprinted (adapted) with permission from ref. 60. Copyright © 2009, American Chemical Society.

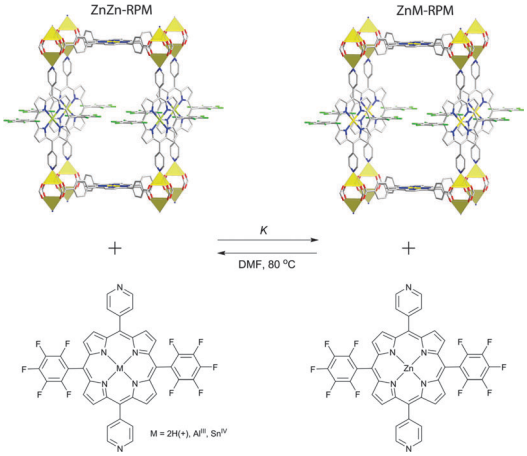


Fig. 29 Pillared-based solvent-assisted linker exchange reactions. Reprinted (adapted) from ref. 66.

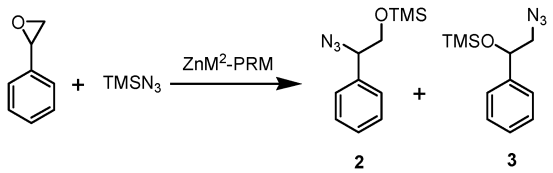


Scheme 3 Ring opening reaction with $TMSN_3$. Reprinted (adapted) from ref. 66.

linker exchange of ZnZn-RPM *via* exchanging dipyridylporphyrin pillars (Fig. 29). This work proves that ZnAl-RPM catalyzes efficiently the ring-opening reaction (Scheme 3), when compared to ZnZn-RPM, Zn2H-RPM, ZnSn-RPM and ZnCo-RMP (Table 3). The catalytic activity is consistent with its relatively strong Lewis acidity.

$CO_2$, the major greenhouse gas suspected of causing global warming, provides an abundant, cheap, and non-toxic renewable C1 building block. Although $CO_2$ capture and sequestration provide adequate methods of mitigating high levels of atmospheric $CO_2$, efficient chemical conversion of $CO_2$ into desirable, economically useful products provides a promising method of recycling and reusing the abundant natural product. In particular, intensive interest lies in cyclic carbonates formed *via* the coupling of epoxide with $CO_2$, given their wide applications

Table 3 Summary of ring-opening reaction data for candidate RPM catalysts.[a] Reprinted (adapted) from ref. 66

| $M^2$ | Conversion[b] (%) | 2/3[b] |
|---|---|---|
| $Zn^{II}$ | 2 | — |
| 2H | <1 | — |
| $Sn^{IV}$ | 2 | — |
| $Al^{III}$ | 60 | 73/27 |
| Co[c] | 6 | 80/20 |

[a] Styrene oxide 15 mg (0.13 mmol), $TMSN_3$ 22 mg (0.19 mmol), $ZnM^2$-RPM 2 mg (0.001 mmol), $CDCl_3$ 5 mL, 20 °C, 18 h. [b] Product ratio (Scheme 3) as determined by $^1H$ NMR. [c] Although introduced as Co(II), in porphyrin coordination environments cobalt is often air-oxidized to Co(III).

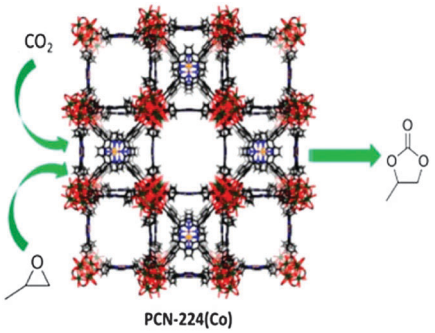


Fig. 30 Cyclic carbonates formed *via* the coupling of epoxide with $CO_2$ catalyzed by PCN-224(Co). Reprinted (adapted) with permission from ref. 68. Copyright © 2013, American Chemical Society.

in pharmaceutical and fine chemical industries. Zhou and co-workers employed PCN-224(Co) as a heterogeneous catalyst in the presence of additives for the production of cyclic carbonates from $CO_2$ and epoxides at 100 °C under the pressure of 2 MPa (Fig. 30).[68] PCN-224(Co) (loaded with ~0.1 mol%) showed catalytic activity, yielding a 42% conversion after 4 hours and demonstrated recyclability after three consecutive catalysis runs. The Lewis acidity should be attributed to two different moieties, the cobalt sites within the porphyrin cores, and the 6-connected $Zr_6$–oxo clusters.

Since Lewis acid sites play a crucial role in this $CO_2$ fixation process, a high density of Lewis acid sites in a confined, accessible nanospace is desirable to promote strongly this reaction. Under this premise, Ma and co-workers made use of *in situ* porphyrin metallation and molecular self-assembly to form MMPF-9, a channeled structure, featuring a high density of Cu(II) sites within the confined nanospace (Fig. 31).[85] MMPF-9 is sustained by a custom-designed octatopic porphyrin ligand

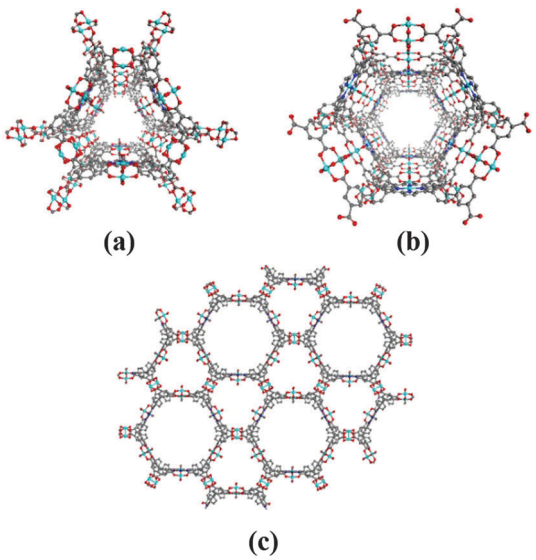


Fig. 31 (a) The truncated triangular channel, (b) the hexagonal channel, and (c) the extended channels of MMPF-9 viewed along the *c*-direction. Reprinted (adapted) from ref. 85.

Table 4 Different substituted epoxides coupled with $CO_2$ catalyzed by MOFs at room temperature under 1 atm pressure. Reprinted (adapted) from ref. 85

| Entry | Epoxides | Products | Yield [%] |
|---|---|---|---|
| 1[a] |  | 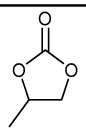 | 87.4 |
| 2[b] |  | 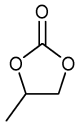 | 49.2 |
| 3[a] | 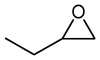 | 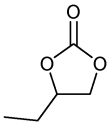 | 80.3 |
| 4[a] | 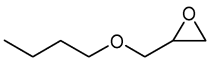 | 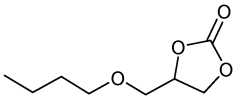 | 30.5 |
| 5[c] | 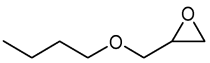 | 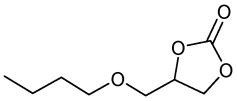 | 65.9 |
| 6[a] | 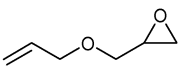 | 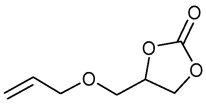 | 29.7 |
| 7[d] |  | 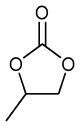 | 86.4 |

[a] Reaction conditions: epoxide (25 mmol) with MMPF-9 (0.03125 mmol), *n*-$Bu_4NBr$, at room temperature under 1 atm $CO_2$ for 48 hours. [b] The same reaction conditions loaded with HKUST-1 (0.03125 mmol). [c] Reaction time was extended to 96 hours under similar conditions. [d] The recyclability test of MMPF-9.

(5,10,15,20-tetrakis(3,5-dicarboxybiphenyl)-porphine, tdcbpp) and copper paddlewheel SBUs, in which the porphyrin ligand is metalated *in situ* with Cu(II) in the same way as those in the SBUs. The high density of open copper sites renders MMPF-9 as a highly efficient heterogeneous catalyst (in the yield of 87.4% over 48 hours) for chemical fixation of $CO_2$ with epoxides at room temperature under 1 atm pressure (Table 4), rather than demanding conditions of high temperature and high pressure. Ambient reaction conditions offer an opportunity to decrease the cost of $CO_2$ fixation and pave an avenue to mitigate $CO_2$ emission in the future.

**4.2.3 Photocatalysis.** It has been well known that many metalloporphyrin present distinct chromophoric properties and photocatalytic activities in the homogeneous phase because of their highly conjugated, aromatic electron system. Thus incorporating metalloporphyrins into robust porous MOFs should display similar chromophoric properties and photocatalytic activities in the heterogeneous phase. In addition to taking advantage of the high surface area of porous materials and the recyclability of heterogeneous catalysts, the

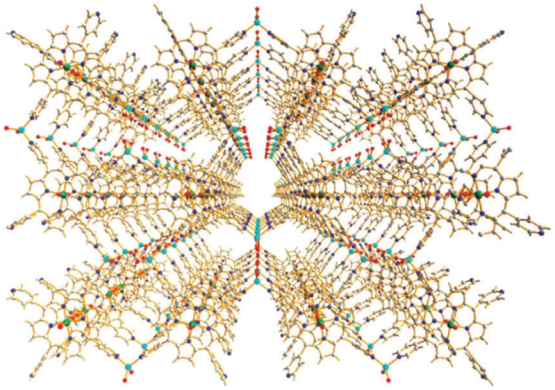

Fig. 32 A perspective view of the 3D framework of $Sn^{IV}$–MOF down the *c* axis. Reprinted (adapted) with permission from ref. 72. Copyright © 2011, American Chemical Society.

inclusion of metalloporphyrins into robust frameworks can also circumvent the degradation issues of the reaction with singlet oxygen.

Wu and co-workers constructed a 3D metalloporphyrin-based framework using a photoactive tin(IV)-based porphyrin ($Sn^{IV}$TPyP) as an MBB.[72] The $Sn^{IV}$TPyP ligands bridge Zn atoms to propagate into 2D sheet-like layers (Fig. 32). These layers are further coupled by formates generated *in situ* to form a 3D network. The immobilization of the photoactive $Sn^{IV}$TPyP allowed further investigation of the 3D framework as an efficient heterogeneous catalyst for photo-oxygenation of 1,4-dihydroxybenzene and sulfides under Xe lamp irradiation. The catalytic activity of this porous solid framework exceeds those of its corresponding homogeneous components. Moreover, this heterogeneous catalyst is easily recovered and reused in successive runs without deterring the catalytic activity.

Rosseinsky and co-workers exploited the visible-light photocatalytic activity of a multicomponent system, composed of a porphyrin-based MOF/ethylenediaminetetracetic acid(EDTA)/colloidal Pt, to evolve hydrogen from water (Fig. 33).[109] The porphyrin-based material, obtained from hydrothermal reaction of $AlCl_3$ and free-base TCPP ligand, afforded a microcrystalline porous MOF, Al-PMOF, with a surface area of ~1400 $m^2$ $g^{-1}$. Furthermore, Al-PMOF exhibited high thermal and chemical stability. The free-base form of Al-PMOF allows postsynthetic insertion of zinc into the porphyrin ring. As the porphyrinic MOFs serve as an antenna to harvest light and inject electrons from the sacrificial electron donor of EDTA to catalytically active centers of Pt, the multicomponent system shows heterogeneous photocatalytic activity, evolving hydrogen from water in the visible light range. This study also proved the ability to tune the photocatalytic functionality by coordinating metal cations within the porphyrin rings.

Extending the above work, Huang and co-workers investigated the enhanced capture and photoreduction of $CO_2$ over a copper-derived Al-PMOF and compared its activity to the free-base Al-PMOF.[111] Copper(II) ions were post-synthetically inserted into porphyrin cores of Al-PMOF, resulting in the copper-derived Al/Cu-PMOF. When compared to Al-PMOF, Al/Cu-PMOF exhibited higher $CO_2$ adsorption uptake due to interactions characterized by FT-IR measurements between $CO_2$ with copper sites within the porphyrin rings (Fig. 34). Furthermore, Al/Cu-PMOF outperforms Al-PMOF on the basis of photocatalytic $CO_2$ reduction in aqueous solution under visible light irradiation. Thus, from the above studies, we deduce the important role that metal cations within the porphyrin rings play in tuning the photocatalytic behavior of porphyrin-derived MOFs.

**4.2.4 Biomimetic catalysis.** Constructing synthetic systems to mimic natural enzymes with high catalytic activity and substrate selectivity has been a sought-after goal in the past few decades. Specifically, heme, an iron-porphyrin derivative, attracts particular interest because it acts as the catalytic center for many enzyme/protein families, including peroxidases, cytochromes, hemoglobins and myoglobins. Our group and Zhou's group independently proposed employing heme-like active centers as structural motifs for the assembly of highly stable porous MOFs that could provide a powerful tool to mimic biological catalysis.[67,79]

Ma and co-workers reported an iron-based porous MMPF, MMPF-6,[79] constructed *via* self-assembly of the iron(III)-metalated TCPP ligand with *in situ* generated $Zr_6O_8(COO)_8(H_2O)_6$ SBU under solvothermal conditions (Fig. 35). Catalytic assays were conducted

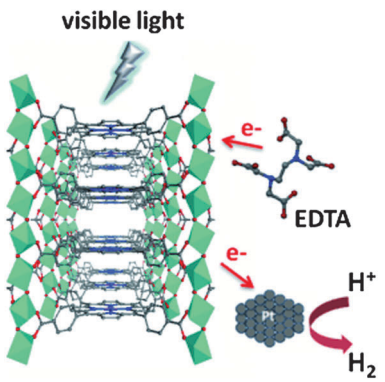


Fig. 33 The photocatalytic reaction using Zn inserted Al-PMOF and colloidal Pt. Reprinted (adapted) with permission from ref. 109. Copyright © 2012 WILEY-VCH Verlag GmbH & Co. KGaA, Weinheim.

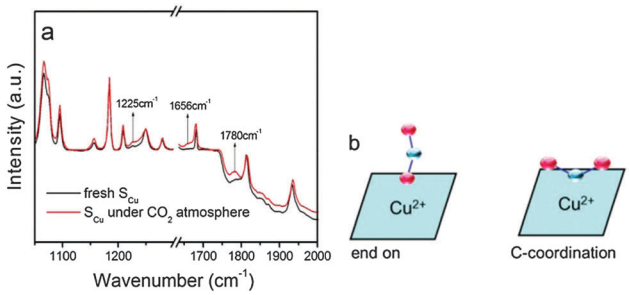


Fig. 34 *In situ* FT-IR spectra of fresh Al/Cu-PMOF and Al/Cu-PMOF under a $CO_2$ atmosphere. (b) Schematic representation of the "end-on" and "C-coordination" adsorption geometry of $CO_2$ on Al/Cu-PMOF. Reprinted (adapted) with permission from ref. 111. Copyright © 2013, American Chemical Society.

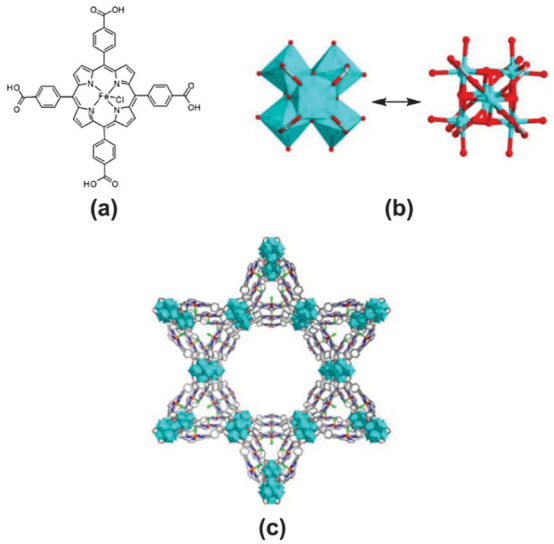


Fig. 35 (a) Iron(III) *meso*-tetrakis(4-carboxyphenyl)porphyrin chloride ligand. (b) $Zr_6O_8(CO_2)_8(H_2O)_8$ SBU. (c) Hexagonal and triangular 1D channels of MMPF-6. Reprinted (adapted) with permission from ref. 79. Copyright © 2012, American Chemical Society.

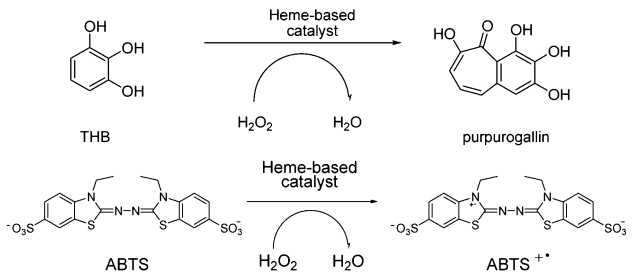


Scheme 4 Reaction schemes for oxidation of THB (top) and ABTS (bottom) by hydrogen peroxide catalyzed by a heme-based catalyst. Reprinted (adapted) with permission from ref. 79. Copyright © 2012, American Chemical Society.

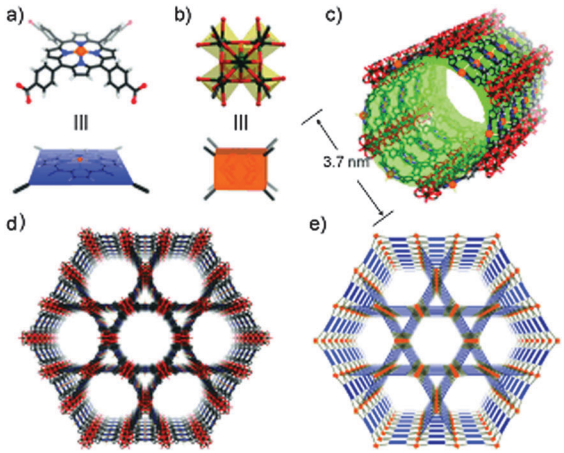


Fig. 36 Crystal structure and underlying network topology of PCN-222(Fe). The Fe-TCPP (a; blue square) is connected to four 8-connected $Zr_6$ clusters (b; light orange cuboid) with a twisted angle to generate a 3D network in Kagome-like topology (d, e) with 1D large channels (c; green pillar). Zr black spheres, C gray, O red, N blue, Fe orange. H atoms were omitted for clarity. Reprinted (adapted) with permission from ref. 67. Copyright © 2012 WILEY-VCH Verlag GmbH & Co. KGaA, Weinheim.

Table 5 Kinetic parameters for the oxidation of substrates by different catalysts

| Substrate | Catalyst | $K_m$/ mM | $k_{cat}$/ $min^{-1}$ | $(k_{cat}/K_m)$/ $M^{-1}$ $min^{-1}$ |
|---|---|---|---|---|
| Pyrogallol | PCN-222(Fe) | 0.33 | 16.1 | $4.85 \times 10^4$ |
| | Hemin | N/A | 2.4 | N/A |
| | HRP | 0.81 | $1.8 \times 10^3$ | $2.20 \times 10^6$ |
| 3,3,5,5-Tetramethylbenzidine | PCN-222(Fe) | 1.63 | 14.0 | $8.59 \times 10^3$ |
| | Hemin | 0.78 | 0.1 | $1.26 \times 10^2$ |
| | HRP | 0.43 | $2.4 \times 10^5$ | $5.58 \times 10^8$ |
| *o*-Phenylenediamine | PCN-222(Fe) | 8.92 | 7.3 | $8.18 \times 10^2$ |
| | Hemin | N/A | 0.8 | N/A |
| | HRP | 0.14 | $3.2 \times 10^4$ | $2.37 \times 10^8$ |

Reprinted (adapted) with permission from ref. 67. Copyright © 2012 WILEY-VCH Verlag GmbH & Co. KGaA, Weinheim.

for MMPF-6 and its corresponding components to examine their peroxidase activity in two experiments used commonly to assess the biomimetic activity of synthetic biocatalysts. Both reactions involve the oxidation of a substrate: the first, the oxidation of 1,2,3-trihydroxybenzene (THB) specifically examines a catalyst's capability to transfer oxygen; while the second reaction, the oxidation of 2,2′-azinodi(3-ethylbenzothiazoline)-6-sulfonate (ABTS) examines electron transfer (Scheme 4). MMPF-6 demonstrated interesting peroxidase-like activity, comparable to the heme protein myoglobin with respect to the initial reaction rates in buffer solution. MMPF-6 also retained the peroxidase activity in an ethanol solution, highlighting its adaptability for organic solvents.

Simultaneously, Zhou and co-workers demonstrated PCN-222(Fe),[67] an isostructure with MMPF-6, possessing large pores (1.3 nm and 3.2 nm) (Fig. 36) and exceptionally high water stability. PCN-222(Fe) exhibited peroxidase-like catalytic oxidation activity toward different substrates, including THB, 3,3,5,5-tetramethylbenzidine and *o*-phenylenediamine (Table 5). However, the inclusion of other metal ions in PCN-222 failed to show significant activity under identical conditions. Thus, the integration of a high density of catalytic centers, large open channels, the inclusion of bio-available metals, and extraordinary chemical stability are the primary factors of building MOF-based platforms for enzyme-mimic catalysis.

The proposed biomimetic catalysis strategy presents distinct advantages unmatched by other strategies. The synthetic MOFs featuring derivatives of enzyme/protein active centers preserve the catalytic activity of those derivatives during the process, preventing the formation of catalytically inactive dimers and the oxidative degradation of the catalysts. While loading heme on supports (zeolites, clays, hydrogels and carbon materials) inevitably dilutes the density of active sites, the synthetic porous MOFs retain the high density of active sites regularly arranged in the accessible channels. Furthermore, the pore structure and chemistry allows for the tuning of the local environment similar to the way a protein matrix creates a different local environment from the bulk solution. These works pave a way to develop MOFs as a new type of biomimetic

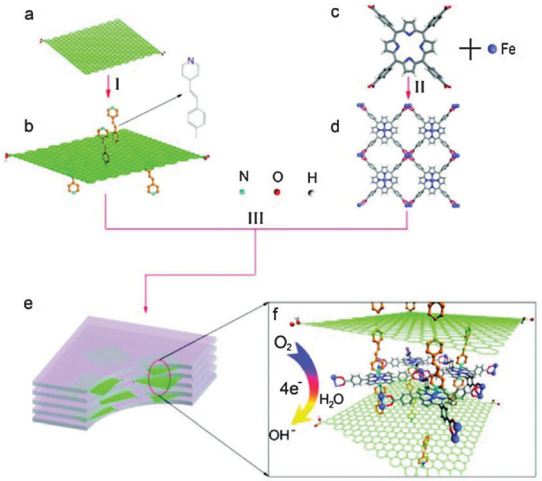


Fig. 37 Schematic representation of the chemical structures of (a) reduced GO (r-GO), (b) G-dye, (c) TCPP, (d) $(Fe–P)_n$ MOF, (e) $(G\text{-dye-FeP})_n$ MOF, and (f) magnified view of layers inside the framework of $(G\text{-dye-FeP})_n$ MOF showing how graphene sheets intercalated between porphyrin networks. Reprinted (adapted) with permission from ref. 112. Copyright © 2012, American Chemical Society.

catalyst and also open up new perspectives for mimicking heme-based proteins.

**4.2.5 Electrocatalysis.** Loh and co-workers studied the electrocatalytic activity of a graphene-porphyrin MOF composite for the cathodic oxygen reduction reaction (ORR).[112] The graphene-porphyrin MOF composite was constructed by the assembly of pyridine-functionalized graphene (reduced graphene oxide), free-based TCPP ligand, and iron(III) salts (Fig. 37). The hybrid composite promoted cathodic oxygen reduction reactions.

Moreover, the electrochemical property of the hybrid material was investigated as a function of weight percentage of functionalized graphene added to the iron-porphyrin framework. The addition of pyridine-functionalized graphene changes the crystallization process of the hybrid composite, increases its porosity (Fig. 38), and enhances the electrochemical charge transfer rate of the iron-porphyrin (Fig. 39). Thus applying the hybrid MOF composite presents a promising facile cathode for four-electron ORR in replacement of platinum-based cathode in an alkaline direct methanol fuel cell.

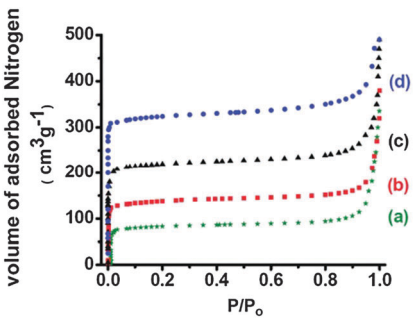


Fig. 38 Nitrogen gas sorption isotherms at 77 K for [green plot (a)] (G-dye 5 wt%-$FeP)_n$ MOF, [red plot (b)] (G-dye 10 wt%-$FeP)_n$ MOF, [black plot (c)] (G-dye 25 wt%-$FeP)_n$ MOF, and [blue plot (d)] (G-dye 50 wt%-$FeP)_n$ MOF. Reprinted (adapted) with permission from ref. 112. Copyright © 2012, American Chemical Society.

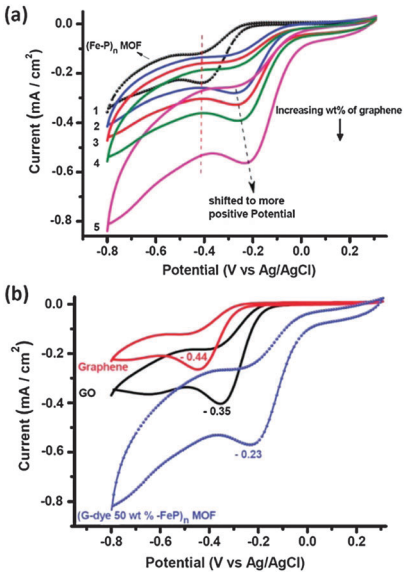


Fig. 39 (a) Cyclic voltammograms of oxygen reduction on the (1) $(Fe–P)_n$ MOF, (2) $(G\text{-dye 5 wt\%-FeP})_n$ MOF, (3) $(G\text{-dye 10 wt\%-FeP})_n$ MOF, (4) $(G\text{-dye 25 wt\%-FeP})_n$ MOF, (5) $(G\text{-dye 50 wt\%-FeP})_n$ MOF electrodes obtained in $O_2$-saturated 0.1 M KOH at a scan rate of 50 mV $s^{-1}$. (b) Cyclic voltammograms of oxygen reduction on (1) exfoliated graphene, (2) GO, (3) $(G\text{-dye 50 wt\%-FeP})_n$ MOF electrodes in 0.1 M KOH $O_2$-saturated at a scan rate of 50 mV $s^{-1}$. Reprinted (adapted) with permission from ref. 112. Copyright © 2012, American Chemical Society.

### 4.3 Nano-thin film

In order to apply MOFs or related coordination materials on nanotechnological devices, their fabrication as nano-thin films has been pursed intensively during the past decade. In particular, controlling the size of objects at the nanoscale and aligning such objects on surfaces of various substances in certain desired ways still remains a challenging issue to be addressed. Among a variety of organic linkers used to fabricate nano-thin films, porphyrin ligands, because of their versatility and functionality, present tremendous potential when combined with suitably chosen active coordination SBUs. Herein, the following efforts specifically focus on how to utilize porphyrins/metalloporphyrins to devise nano-thin films, and the applications of those nano-thin films.

Until recently, only a limited number of studies had examined the fabrication of porphyrin/metalloporphyrin-derived thin films, although they have not paralleled the huge family of porphyrin/metalloporphyrin-based MOFs. In 2010, H. Kitagawa and co-workers reported the facile bottom-up fabrication of a preferentially oriented MOF nanofilm on the surface of a silicon substrate (NAFS-1) at ambient temperature (Fig. 40).[88] NAFS-1 consists of 2D sheets formed from Co-based TCPP interconnected with copper paddlewheel SBUs. Additionally, pyridine pillaring molecules coordinate axially to both the cobalt and copper open centers. The unique integration of the layer-by-layer growth procedure coupled with the Langmuir–Blodgett

 

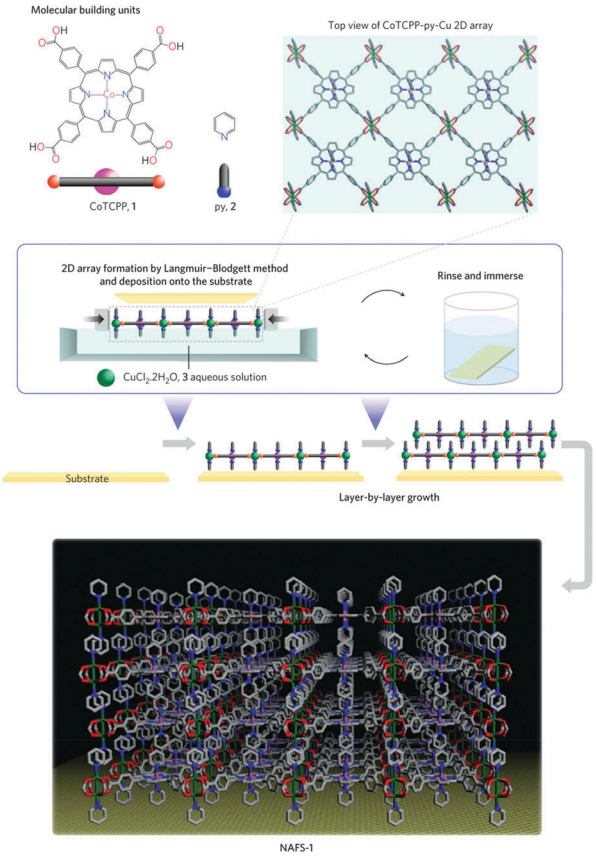


Fig. 40 Schematic illustration of the fabrication method of NAFS-1. Reprinted (adapted) with permission from ref. 88. Copyright © 2010, rights managed by Nature Publishing Group.

method proved an effective protocol to create crystalline MOF nanofilms. This also allowed the generation of NAFS-1 of any desired thickness. By changing the molecular building components (in absence of pillaring pyridine), Kitagawa and co-workers tuned successfully the interlayer spacing of the nanofilm using a similar protocol, resulting in NAFS-2 nanofilm growth deposited on gold or silicon substrates (Fig. 41).[89] Synchrotron X-ray surface crystallography demonstrated that NAFS-1 and NAFS-2 are endowed with highly crystalline order in both the out-of-plane and in-plane orientations with respect to the substrates. In the

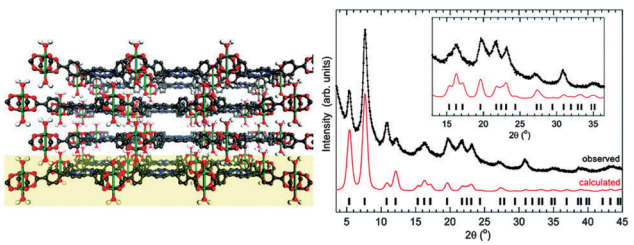


Fig. 41 Schematic diagram of the proposed crystalline structure of NAFS-2 (left) and synchrotron XRD profiles (black circles, $\lambda$ = 1.555 Å) of a NAFS-2 thin film on a gold substrate obtained the in-plane direction with a detection angle of 0.21° with respect to the surface (right). Reprinted (adapted) with permission from ref. 89. Copyright © 2011, American Chemical Society.

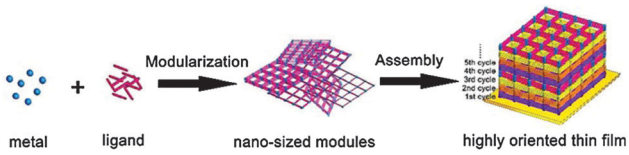


Fig. 42 Illustration of the modular assembly process of the MOF nano-thin film. Reprinted (adapted) with permission from ref. 90. Copyright © 2012, American Chemical Society.

growth of NAFS-1, the metal-coordinated pyridine molecules were proposed to allow each further layers to dock in a highly ordered interdigitated manner. Conversely, in the case of NAFS-2, every monolayer stacked with each other without pillaring units, yet the nanofilm retained high crystallinity order above 200 °C.

In 2012, Kitagawa and co-workers reported a stepwise facile strategy of "modular assembly" for quick construction of a highly oriented crystalline MOF nanofilm (Fig. 42).[90] The initial "modularization" step consists of bulk MOF synthesis conducted under solvothermal conditions with the goal of building up crystalline MOFs modules. The nano-thin films were then assembled *via* a simple and rapid stamping procedure on various substrates under ambient conditions. The MOF thin films prepared through this strategy possessed high crystallinity, controlled orientation and tunable thickness. Furthermore, the modular assembly strategy allows different individual layers featuring different functionalities to be integrated together with the aim of forming hybrid MOF nano-thin films for practical applications.

By virtue of the above modular assembly strategy, Kitagawa and co-workers fabricated the pre-synthesized MOF nanosheet (Cu-TCPP) on the surface of certain electrodes, forming layer-by-layer nano-thin films.[91] The electrical properties of the highly oriented and crystalline MOF nanofilm were studied for the first time. The proton conductivity of this nanofilm stands among the highest reported values for MOF materials. The proton conductivity at certain temperatures varied along with changing relative humidity (RH). At 98% RH the measured proton conductivity value of $3.9 \times 10^{-3}$ S cm$^{-1}$ exceeds the conductivity value of all hydrated MOF samples and compares to the proton conductivity of acid-impregnated MOF materials. This was interpreted by the highly oriented packing of the nanosheet with numerous coordination water and other functional groups on the surface. Thus, the surface of the nanocrystals plays a decisive role in proton conductivity when the size of MOF crystals is decreased to the nanoscale.

In 2013, Hupp and co-workers demonstrated the synthesis and characterization of two thin films (DA-MOF and L2-MOF) of porphyrin-based MOFs on functionalized surfaces of flat silicon and indium tin oxide (ITO) platforms using a layer-by-layer approach (Fig. 43).[64] Profilometry measurements confirm that the thickness of the films is readily controlled *via* the number of assembly cycles. That the porphyrin units are oriented preferentially in both thin films is indicated by polarization excitation and fluorescence measurements. X-Ray reflectivity scans point to

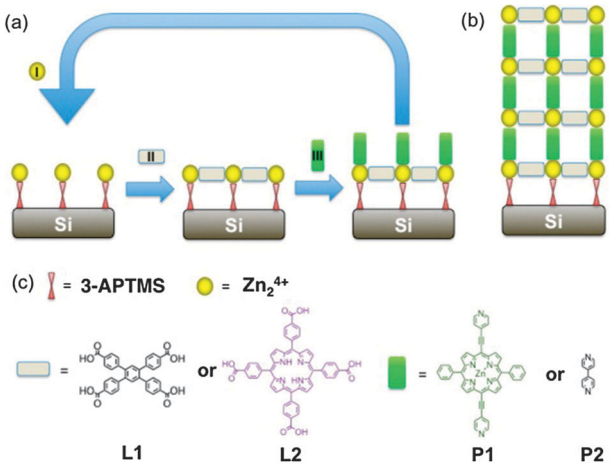


Fig. 43 (a) Schematic diagram for the step-by-step growth of the DA-MOF and L2-MOF structures on idealized 3-APTMS, resulting in (b) a film after *N* cycles of growth. (c) Representations of building blocks used in fabrication of MOF film. Reprinted (adapted) with permission from ref. 64. Copyright © 2013, American Chemical Society.

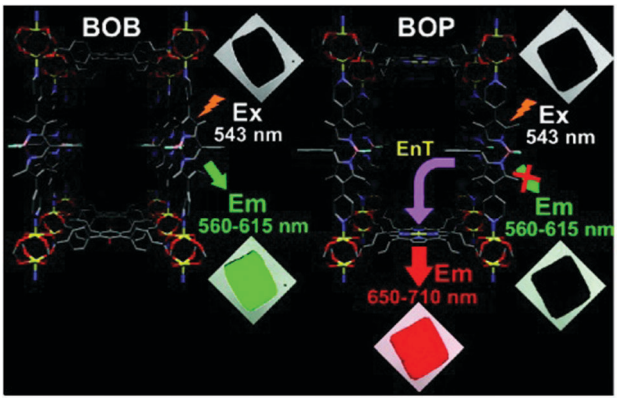


Fig. 44 Confocal laser scanning microscopy (CLSM) images of crystals of: (a) BOB MOF and (b) BOP MOF. For illustrative purposes, when the crystals are shown as black, there is no emission. To denote emission in the "green" and "red" ranges, the remaining crystals are artificially colored green and red, respectively. Reprinted (adapted) with permission from ref. 62. Copyright © 2011, American Chemical Society.

the periodic ordering in the direction normal to the film support and the high porosity of the DA-MOF film is revealed by infiltrating EtOH and DMF into the pores. The relatively milder synthesis conditions permit direct incorporation of free-base porphyrins into the thin films. Long-range energy transfer is demonstrated by photophysical studies with these porphyrinic MOF films and thus offers meaningful insights for the potential utility of porphyrin-based MOF films for light-harvesting and energy transfer in solar energy conversion devices.

### 4.4 Light harvesting

In nature, photon collection and subsequent energy migration from antenna chromophores to reaction centers are primary factors in the conversion of sunlight to chemical energy through photosynthesis. Highly ordered pigment–protein complexes at the nanoscale are employed to accomplish the intricate and delicate processes of light harvesting and subsequent energy transfer with extraordinary efficiency in natural systems. To mimic such highly optimized natural processes, highly ordered porphyrin/metalloporphyrin-based MOFs offer potential modular blueprints integrated with unique chromophoric properties to investigate and target artificial light-harvesting antenna assemblies. Hupp and co-workers have made remarkable contributions to the development of metalloporphyrin-based frameworks for light harvesting applications.

In 2011, efficient single-step excitonic energy transfer was observed in a well-organized donor–acceptor pair in a pillared-layer type MOF (BOP) incorporating bodipy- and porphyrin-based struts.[62] Light harvesting properties were investigated on BOP MOF and the control group of BOB MOF. The studies found that cooperative energy transfer exists from bodipy to the porphyrinic struts of BOP MOF, where the bodipy struts serve as light harvesting antenna chromophores for the excitation of porphyrinic struts (Fig. 44). Meanwhile, the two chromophoric components incorporated in dark-colored BOP MOF crystals are capable of adsorbing light across the entire visible spectrum (Fig. 45).

In 2012, the first example of directional, long-distance energy migration within MOFs was reported.[65] Two MOFs (F-MOF and DA-MOF) are constructed using zinc-metalated bipyridineporphyrin molecules as pillars (Fig. 46). Based on quenching measurements, it is observed that the exciton can visit ~90 porphyrin linkers in DA-MOF and ~6 in F-MOF within the brief exciton lifetime. The remarkable efficient exciton migration in DA-MOF is ascribed to enhanced conjugation *via* the two additional acetylene moieties in the porphyrin molecule, which, in turn, causes greater Q-band absorption intensity and much faster exciton-hopping. Moreover, the theoretical calculation demonstrates that the exciton migration is substantially anisotropic. In total, the distance, efficiency and directionality of energy transfer are exploited in detail in this system, presenting important guidelines for the design of light harvesting antenna.

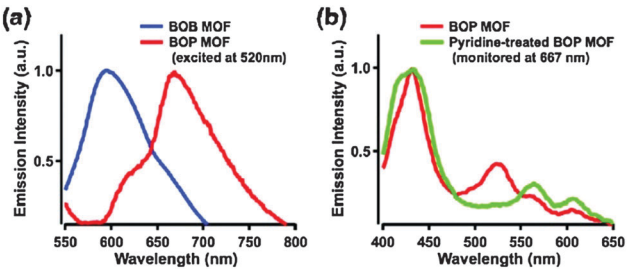


Fig. 45 (a) Emission spectra of BOB and BOP MOFs. Spectra were obtained by excitation at 520 nm. (b) Excitation spectra of BOP and pyridine-treated BOP MOF. Spectra were obtained by scanning the excitation wavelength from 400 to 650 nm, with fixed emission detection at 667 nm. Reprinted (adapted) with permission from ref. 62. Copyright © 2011, American Chemical Society.

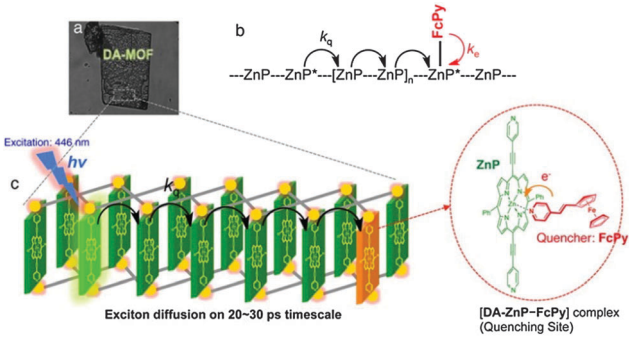


Fig. 46 (a) Photograph of a DA-MOF particle from which fluorescence is recorded based on laser excitation at 446 nm. (b, c) Schematic representation of the exciton migration and quenching processes. Reprinted (adapted) with permission from ref. 65. Copyright © 2013, American Chemical Society.

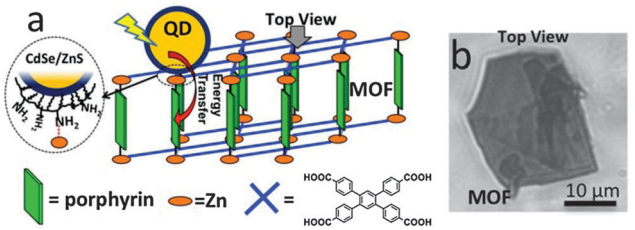


Fig. 47 (a) Schematic diagram of a QD–MOF complex and (b) optical microscopy image of a plate-shaped MOF particle. Reprinted (adapted) with permission from ref. 63. Copyright © 2013, American Chemical Society.

In order to enhance the efficiency of light harvesting across the entire solar spectrum, the porphyrin-based MOFs (F-MOF and DA-MOF) are functionalized with CdSe–ZnS core–shell quantum dots (QDs) (Fig. 47).[63] The QDs are designed to harvest photons in a certain region where the MOFs have little absorption. The photon-promoted excitons in QDs then migrate to the MOFs. The broad absorption band of the QDs in the visible range enables greater coverage of the solar spectrum by QDs–MOF hybrid materials. In this work, time-resolved fluorescence measurements prove that energy transfer to the MOFs upon photoexcitation of QDs occurs with efficiencies of more than 80%. Therefore, this study opens up a new pathway to utilize QDs to compensate the narrow absorption range of chromophoric porphyrins and to develop QDs–MOFs hybrid materials for efficient light harvesting systems.

## 5. Concluding remarks and future prospects

While the area of porphyrin/metalloporphyrin-based MOFs compose only a small part of the broad family of MOFs, over the past few years, the area has made a resurgence, attracting significant interest and forming a distinctive niche because of the unique chemical and biological features exhibited by porphyrin or metalloporphyrin molecules. Crystal engineering allows us the ability to control the spatial arrangement of porphyrins and the local environment around porphyrin molecules. Furthermore, taking a lesson from nature, porphyrins, through the coordination of different transition metals within the ring, provide a tunable platform to carry out a wide variety of functions ranging from gas storage to electron transfer to catalysis. Porphyrin/metalloporphyrin-based crystalline MOFs provide a platform for in-depth investigations between structure–function relationships, allowing insight to further optimize the design of materials for a broad range of specific purposes. As this review demonstrates, porphyrin-based MOFs cover a wide scope of applications, although all domains require further research and development before they become practical in industrial or large scale settings.

This review provides a holistic and systematic overview of the rapid growth metalloporphyrin-based MOFs have seen from first publication to the most recent. We also briefly detail strategies and methods for constructing metalloporphyrin-based frameworks, that is, in connection with the use of these strategies in rational design and targeted synthesis of these frameworks. Specifically, we present examples of crystal engineering strategy, the synthesis of pillared-layers, the formation of nanoscopic metal–organic polyhedral SBBs, and post-synthetic modification as methods allowing rational design of porphyrin/metalloporphyrin based MOFs. In consequence, these strategies open the door for the targeted design of specific frameworks for practical applications.

Significant emphasis focuses on the versatile applications of metalloporphyrin-derived MOFs, including guest molecules adsorption and separation, catalysis, nano-thin films, and light harvesting. Since a large number of MMPFs fail to maintain structural integrity after solvent removal, the synthesis of highly stable MMPFs, capable of preserving crystallinity upon solvent removal, presents one of the obstacles to be overcome. Although the high cost of MMPFs may seem to hinder their applications for gas adsorption and separation, the high density of accessible metal sites and favorable interactions between gas molecules and metalloporphyrins justify a demand for further development of porous porphyrin-based frameworks featuring high surface areas and remarkable stabilities. Porous MMPF materials can merge their porosity with other functionalities for the construction of multifunctional porphyrinic materials.

Currently, MMPFs are most extensively studied as heterogeneous catalytic systems. Incorporating catalytically active metalloporphyrin struts into the frameworks achieves highly efficient size- and shape-selective heterogeneous catalysis due to the high density of metalloporphyrin active sites confined in the nanospace. Furthermore, the biological role metalloporphyrins play in nature motivates chemists to mimic the enzyme-like centers in the metalloporphyrin framework platforms with the goal achieving high activity and substrate selectivity under mild conditions. The crystalline nature of MOFs and well developed engineering strategies create the opportunity to design and investigate systematically frameworks that mimic protein and enzyme matrices and catalytically active centers.

Outside of catalysis, the conversion of solar energy to electrical or chemical energy presents a promising target for highly ordered metalloporphyrin frameworks. Metalloporphyrins, with a unique, highly conjugated, aromatic electron system, have the potential to absorb essentially the entire visible spectrum. The accomplished studies facilitate better understanding toward light harvesting and energy transfer and stimulate further interest. Additionally, nano-thin film fabrication expands the number of applications and brings about the opportunity to utilize metalloporphyrinic frameworks for specific applications such as photovoltaic devices.

In summary, resurging as a unique type of functional porous materials, metalloporphyrin-based MOFs will continue to draw interest and inquiry by both academia and industry as they possess unique and distinctive features. It is an understatement to predict that MMPFs have a promising future for practical applications. However, with the field still budding, we still cannot conceive an exhaustive picture of the fruit metalloporphyrin-based MOFs will produce.

## Acknowledgements

The authors acknowledge the University of South Florida for financial support of this work. An award from the National Science Foundation (DMR-1352065) is also acknowledged.

## Notes and references

1 J. R. Long and O. M. Yaghi, *Chem. Soc. Rev.*, 2009, **38**, 1213–1214.
2 L. R. MacGillivray, *Metal-Organic Frameworks: Design and Application*, Wiley, 1 edn 2010.
3 H.-C. Zhou, J. R. Long and O. M. Yaghi, *Chem. Rev.*, 2012, **112**, 673–674.
4 C. M. Drain, A. Varotto and I. Radivojevic, *Chem. Rev.*, 2009, **109**, 1630–1658.
5 K. M. Kadish, K. M. Smith and R. Guilard, *The Porphyrin Handbook*, Academic Press, San Diego, 2000–2003.
6 I. Beletskaya, V. S. Tyurin, A. Y. Tsivadze, R. Guilard and S. Christine, *Chem. Rev.*, 2009, **109**, 1659–1713.
7 Y. Nakamura, N. Aratani and A. Osuka, *Chem. Soc. Rev.*, 2007, **36**, 831–845.
8 B. F. Abrahams, B. F. Hoskins and R. Robson, *J. Am. Chem. Soc.*, 1991, **113**, 3606–3607.
9 S. S.-Y. Chui, S. M.-F. Lo, J. P. H. Charmant, A. G. Orpen and I. D. Williams, *Science*, 1999, **283**, 1148–1150.
10 H. Li, M. Eddaoudi, M. O'Keeffe and O. M. Yaghi, *Nature*, 1999, **402**, 276–279.
11 E. B. Fleischer and A. M. Shachter, *Inorg. Chem.*, 1991, **30**, 3763–3769.
12 H. Krupitshy, Z. Stein and I. Goldberg, *J. Inclusion Phenom. Mol. Recognit. Chem.*, 1994, **18**, 177–192.
13 R. K. Kumar, S. Balasubramanian and I. Goldberg, *Chem. Commun.*, 1998, 1435–1436.
14 R. K. Kumar, S. Balasubramanian and I. Goldberg, *Inorg. Chem.*, 1998, **37**, 541–552.
15 R. K. Kumar, S. Balasubramanian and I. Goldberg, *Mol. Cryst. Liq. Cryst. Sci. Technol., Sect. A*, 1998, **313**, 105–114.
16 R. K. Kumar and I. Goldberg, *Angew. Chem., Int. Ed.*, 1998, **37**, 3027–3030.
17 Y. Diskin-Posner, S. Dahal and I. Goldberg, *Angew. Chem., Int. Ed.*, 2000, **39**, 1288–1292.
18 Y. Diskin-Posner, S. Dahal and I. Goldberg, *Chem. Commun.*, 2000, 585–586.
19 I. Goldberg, *Chem. – Eur. J.*, 2000, **6**, 3863–3870.
20 Y. Diskin-Posner and I. Goldberg, *New J. Chem.*, 2001, **25**, 899–904.
21 Y. Diskin-Posner, G. K. Patra and I. Goldberg, *Eur. J. Inorg. Chem.*, 2001, 2515–2523.
22 Y. Diskin-Posner, G. K. Patra and I. Goldberg, *J. Chem. Soc., Dalton Trans.*, 2001, 2775–2782.
23 M. Shmilovits, Y. Diskin-Posner, M. Vinodu and I. Goldberg, *Cryst. Growth Des.*, 2003, **3**, 855–863.
24 M. Shmilovits, M. Vinodu and I. Goldberg, *Cryst. Growth Des.*, 2004, **4**, 633–638.
25 M. Shmilovits, M. Vinodu and I. Goldberg, *New J. Chem.*, 2004, **28**, 223–227.
26 M. Vinodu and I. Goldberg, *New J. Chem.*, 2004, **28**, 1250.
27 I. Goldberg, *Chem. Commun.*, 2005, 1243–1254.
28 S. George, S. Lipstman and I. Goldberg, *Cryst. Growth Des.*, 2006, **6**, 2651–2654.
29 S. George, S. Lipstman, S. Muniappan and I. Goldberg, *CrystEngComm*, 2006, **8**, 417–424.
30 S. Lipstman, S. Muniappan, S. George and I. Goldberg, *Dalton Trans.*, 2007, 3273–3281.
31 S. Muniappan, S. Lipstman, S. George and I. Goldberg, *Inorg. Chem.*, 2007, **46**, 5544–5554.
32 I. Goldberg, *CrystEngComm*, 2008, **10**, 637–645.
33 S. Lipstman and I. Goldberg, *J. Mol. Struct.*, 2008, **890**, 101–106.
34 S. Lipstman and I. Goldberg, *Beilstein J. Org. Chem.*, 2009, **5**, 77.
35 A. Karmakar and I. Goldberg, *CrystEngComm*, 2010, **12**, 4095–4100.
36 S. Lipstman and I. Goldberg, *CrystEngComm*, 2010, **12**, 52–54.
37 S. Lipstman and I. Goldberg, *Cryst. Growth Des.*, 2010, **10**, 1823–1832.
38 S. Lipstman and I. Goldberg, *Cryst. Growth Des.*, 2010, **10**, 5001–5006.
39 S. Lipstman and I. Goldberg, *Cryst. Growth Des.*, 2010, **10**, 4596–4606.
40 S. Lipstman and I. Goldberg, *Cryst. Growth Des.*, 2013, **13**, 942–952.
41 M. E. Kosal and K. S. Suslick, *J. Solid State Chem.*, 2000, **152**, 87–98.
42 M. E. Kosal, J.-H. Chou and K. S. Suslick, *J. Porphyrins Phthalocyanines*, 2002, **6**, 377–381.
43 M. E. Kosal, J.-H. Chou, S. R. Wilson and K. S. Suslick, *Nat. Mater.*, 2002, **1**, 118–121.

 

44 D. W. Smithenry, S. R. Wilson and K. S. Suslick, *Inorg. Chem.*, 2003, **42**, 7719–7721.
45 K. S. Suslick, P. Bhyrappa, J.-H. Chou, M. E. Kosal, S. Nakagaki, D. W. Smithenry and S. R. Wilson, *Acc. Chem. Res.*, 2005, **38**, 283–291.
46 E.-Y. Choi, P. M. Barron, R. W. Novotney, C. Hu, Y.-U. K. Kwon and W. Choe, *CrystEngComm*, 2008, **10**, 824–826.
47 P. M. Barron, H.-T. Son, C. Hu and W. Choe, *Cryst. Growth Des.*, 2009, **9**, 1960–1965.
48 E.-Y. Choi, P. M. Barron, R. W. Novotny, H.-T. Son, C. Hu and W. Choe, *Inorg. Chem.*, 2009, **48**, 426–428.
49 E.-Y. Choi, C. A. Wray, C. Hu and W. Choe, *CrystEngComm*, 2009, **11**, 553–555.
50 H. Chung, P. M. Barron, R. W. Novotny, H.-T. Son, C. Hu and W. Choe, *Cryst. Growth Des.*, 2009, **9**, 3327–3332.
51 L. D. DeVries and W. Choe, *J. Chem. Crystallogr.*, 2008, **39**, 229–240.
52 J. M. Verduzco, H. Chung, C. Hu and W. Choe, *Inorg. Chem.*, 2009, **48**, 9060–9062.
53 P. M. Barron, C. A. Wray, C. Hu, Z. Guo and W. Choe, *Inorg. Chem.*, 2010, **49**, 10217–10219.
54 E.-Y. Choi, L. D. DeVries, R. W. Novotny, C. Hu and W. Choe, *Cryst. Growth Des.*, 2010, **10**, 171–176.
55 B. J. Burnett, P. M. Barron, C. Hu and W. Choe, *J. Am. Chem. Soc.*, 2011, **133**, 9984–9987.
56 L. D. DeVries, P. M. Barron, E. P. Hurley, C. Hu and W. Choe, *J. Am. Chem. Soc.*, 2011, **133**, 14848–14851.
57 B. J. Burnett, P. M. Barron and W. Choe, *CrystEngComm*, 2012, **14**, 3839–3846.
58 B. J. Burnett and W. Choe, *Dalton Trans.*, 2012, **41**, 3889–3894.
59 B. J. Burnett and W. Choe, *CrystEngComm*, 2012, **14**, 6129–6131.
60 A. M. Shultz, O. K. Farha, J. T. Hupp and S. T. Nguyen, *J. Am. Chem. Soc.*, 2009, **131**, 4204–4205.
61 O. K. Farha, A. M. Shultz, A. A. Sarjeant, S. T. Nguyen and J. T. Hupp, *J. Am. Chem. Soc.*, 2011, **133**, 5652–5655.
62 C. Y. Lee, O. K. Farha, B. J. Hong, A. A. Sarjeant, S. T. Nguyen and J. T. Hupp, *J. Am. Chem. Soc.*, 2011, **133**, 15858–15861.
63 S. Jin, H.-J. Son, O. K. Farha, G. P. Wiederrecht and J. T. Hupp, *J. Am. Chem. Soc.*, 2013, **135**, 955–958.
64 M. C. So, S. Jin, H.-J. Son, G. P. Wiederrecht, O. K. Farha and J. T. Hupp, *J. Am. Chem. Soc.*, 2013, **135**, 15698–15701.
65 H.-J. Son, S. Jin, S. Patwardhan, S. J. Wezenberg, N. C. Jeong, M. So, C. E. Wilmer, A. A. Sarjeant, G. C. Schatz, R. Q. Snurr, O. K. Farha, G. P. Wiederrecht and J. T. Hupp, *J. Am. Chem. Soc.*, 2013, **135**, 862–869.
66 S. Takaishi, E. J. DeMarco, M. J. Pellin, O. K. Farha and J. T. Hupp, *Chem. Sci.*, 2013, **4**, 1509–1513.
67 D. Feng, Z.-Y. Gu, J.-R. Li, H.-L. Jiang, Z. Wei and H.-C. Zhou, *Angew. Chem., Int. Ed.*, 2012, **51**, 10307–10310.
68 D. Feng, W.-C. Chung, Z. Wei, Z.-Y. Gu, H.-L. Jiang, Y.-P. Chen, D. J. Darensbourg and H.-C. Zhou, *J. Am. Chem. Soc.*, 2013, **135**, 17105–17110.
69 D. Feng, H.-L. Jiang, Y.-P. Chen, Z.-Y. Gu, Z. Wei and H.-C. Zhou, *Inorg. Chem.*, 2013, **52**, 12661–12667.
70 H.-L. Jiang, D. Feng, K. Wang, Z.-Y. Gu, Z. Wei, Y.-P. Chen and H.-C. Zhou, *J. Am. Chem. Soc.*, 2013, **135**, 13934–13938.
71 M.-H. Xie, X.-L. Yang and C.-D. Wu, *Chem. Commun.*, 2011, **47**, 5521–5523.
72 M.-H. Xie, X.-L. Yang, C. Zou and C.-D. Wu, *Inorg. Chem.*, 2011, **50**, 5318–5320.
73 X.-L. Yang, M.-H. Xie, C. Zou, Y. He, B. Chen, M. O'Keeffe and C.-D. Wu, *J. Am. Chem. Soc.*, 2012, **134**, 10638–10645.
74 C. Zou and C.-D. Wu, *Dalton Trans.*, 2012, **41**, 3879–3888.
75 C. Zou, M.-H. Xie, G.-Q. Kong and C.-D. Wu, *CrystEngComm*, 2012, **14**, 4850–4856.
76 C. Zou, Z. Zhang, X. Xu, Q. Gong, J. Li and C.-D. Wu, *J. Am. Chem. Soc.*, 2012, **134**, 87–90.
77 M.-H. Xie, X.-L. Yang, Y. He, J. Zhang, B. Chen and C.-D. Wu, *Chem. – Eur. J.*, 2013, **19**, 14316–14321.
78 X.-S. Wang, L. Meng, Q. Cheng, C. Kim, L. Wojtas, M. Chrzanowski, Y.-S. Chen, X. P. Zhang and S. Ma, *J. Am. Chem. Soc.*, 2011, **133**, 16322–16325.
79 Y. Chen, T. Hoang and S. Ma, *Inorg. Chem.*, 2012, **51**, 12600–12602.
80 L. Meng, Q. Cheng, C. Kim, W.-Y. Gao, L. Wojtas, Y.-S. Chen, M. J. Zaworotko, X. P. Zhang and S. Ma, *Angew. Chem., Int. Ed.*, 2012, **51**, 10082–10085.
81 X.-S. Wang, M. Chrzanowski, W.-Y. Gao, L. Wojtas, Y.-S. Chen, M. J. Zaworotko and S. Ma, *Chem. Sci.*, 2012, **3**, 2823–2827.
82 X.-S. Wang, M. Chrzanowski, C. Kim, W.-Y. Gao, L. Wojtas, Y.-S. Chen, X. Peter Zhang and S. Ma, *Chem. Commun.*, 2012, **48**, 7173–7175.
83 W.-Y. Gao, Z. Zhang, L. Cash, L. Wojtas, Y.-S. Chen and S. Ma, *CrystEngComm*, 2013, **15**, 9320–9323.
84 X.-S. Wang, M. Chrzanowski, L. Wojtas, Y.-S. Chen and S. Ma, *Chem. – Eur. J.*, 2013, **19**, 3297–3301.
85 W.-Y. Gao, L. Wojtas and S. Ma, *Chem. Commun.*, 2014, DOI: 10.1039/c3cc47542e.
86 B. F. Abrahams, B. F. Hoskins, D. M. Michail and R. Robson, *Nature*, 1994, **369**, 727–729.
87 R. Makiura and H. Kitagawa, *Eur. J. Inorg. Chem.*, 2010, 3715–3724.
88 R. Makiura, S. Motoyama, Y. Umemura, H. Yamanaka, O. Sakata and H. Kitagawa, *Nat. Mater.*, 2010, **9**, 565–571.
89 S. Motoyama, R. Makiura, O. Sakata and H. Kitagawa, *J. Am. Chem. Soc.*, 2011, **133**, 5640–5643.
90 G. Xu, T. Yamada, K. Otsubo, S. Sakaida and H. Kitagawa, *J. Am. Chem. Soc.*, 2012, **134**, 16524–16527.
91 G. Xu, K. Otsubo, T. Yamada, S. Sakaida and H. Kitagawa, *J. Am. Chem. Soc.*, 2013, **135**, 7438–7441.
92 K.-J. Lin, *Angew. Chem., Int. Ed.*, 1999, **38**, 2730–2732.
93 B. Zimmer, V. Bulach, M. W. Hosseini, A. De Cian and N. Kyritsakas, *Eur. J. Inorg. Chem.*, 2002, 3079–3082.
94 E. Deiters, V. Bulach and M. W. Hosseini, *Dalton Trans.*, 2007, 4126–4131.
95 S. K. Taylor, G. B. Jameson and P. D. W. Boyd, *Supramol. Chem.*, 2005, **17**, 543–546.
96 J. Bhuyan and S. Sarkar, *Cryst. Growth Des.*, 2011, **11**, 5410–5414.

97 W.-T. Chen, Y. Yamada, G.-N. Liu, A. Kubota, T. Ichikawa, Y. Kojima, G.-C. Guo and S. Fukuzumi, *Dalton Trans.*, 2011, **40**, 12826–12831.
98 S. Matsunaga, N. Endo and W. Mori, *Eur. J. Inorg. Chem.*, 2011, 4550–4557.
99 F. Sguerra, V. Bulach and M. W. Hosseini, *Dalton Trans.*, 2012, **41**, 14683–14689.
100 J. A. Johnson, Q. Lin, L.-C. Wu, N. Obaidi, Z. L. Olson, T. C. Reeson, Y.-S. Chen and J. Zhang, *Chem. Commun.*, 2013, **49**, 2828–2830.
101 S. Matsunaga, S. Kato, N. Endo and W. Mori, *Chem. Lett.*, 2013, **42**, 298–300.
102 Q. Zha, C. Ding, X. Rui and Y. Xie, *Cryst. Growth Des.*, 2013, **13**, 4583–4590.
103 B. Moulton and M. J. Zaworotko, *Chem. Rev.*, 2001, **101**, 1629–1658.
104 G. R. Desiraju, *Angew. Chem., Int. Ed.*, 2007, **46**, 8342–8356.
105 D. Sun, F. S. Tham, C. A. Reed and P. D. W. Boyd, *Proc. Natl. Acad. Sci. U. S. A.*, 2002, **99**, 5088–5092.
106 W. Morris, B. Volosskiy, S. Demir, F. Gándara, P. L. McGrier, H. Furukawa, D. Cascio, J. F. Stoddart and O. M. Yaghi, *Inorg. Chem.*, 2012, **51**, 6443–6445.
107 T. Ohmura, A. Usuki, K. Fukumori, T. Ohta, M. Ito and K. Tatsumi, *Inorg. Chem.*, 2006, **45**, 7988–7990.
108 A. Fateeva, S. Devautour-Vinot, N. Heymans, T. Devic, J.-M. Grenèche, S. Wuttke, S. Miller, A. Lago, C. Serre, G. De Weireld, G. Maurin, A. Vimont and G. Férey, *Chem. Mater.*, 2011, **23**, 4641–4651.
109 A. Fateeva, P. A. Chater, C. P. Ireland, A. A. Tahir, Y. Z. Khimyak, P. V. Wiper, J. R. Darwent and M. J. Rosseinsky, *Angew. Chem., Int. Ed.*, 2012, **51**, 7440–7444.
110 S. Matsunaga, N. Endo and W. Mori, *Eur. J. Inorg. Chem.*, 2012, 4885–4897.
111 Y. Liu, Y. Yang, Q. Sun, Z. Wang, B. Huang, Y. Dai, X. Qin and X. Zhang, *ACS Appl. Mater. Interfaces*, 2013, **5**, 7654–7658.
112 M. Jahan, Q. Bao and K. P. Loh, *J. Am. Chem. Soc.*, 2012, **134**, 6707–6713.

 